PHOTONICS Research

Mid-infrared silicon photonic waveguides and devices [Invited]

Yi Zou,[1,2,*] Swapnajit Chakravarty,[3] Chi-Jui Chung,[2] Xiaochuan Xu,[3] and Ray T. Chen[2,3,4]

[1]School of Information Science and Technology, ShanghaiTech University, Shanghai 201210, China
[2]Microelectronic Research Center, Department of Electrical and Computer Engineering, University of Texas, Austin, Texas 78758, USA
[3]Omega Optics, Inc., 8500 Shoal Creek Boulevard, Austin, Texas 78757, USA
[4]e-mail: chenrt@austin.utexas.edu
*Corresponding author: zouyi@shanghaitech.edu.cn

Received 6 September 2017; revised 6 January 2018; accepted 10 January 2018; posted 10 January 2018 (Doc. ID 306245); published 22 March 2018

Silicon has been the material of choice of the photonics industry over the last decade due to its easy integration with silicon electronics, high index contrast, small footprint, and low cost, as well as its optical transparency in the near-infrared and parts of mid-infrared (MIR) wavelengths (from 1.1 to 8 μm). While considerations of micro- and nano-fabrication-induced device parameter deviations and a higher-than-desirable propagation loss still serve as a bottleneck in many on-chip data communication applications, applications as sensors do not require similar stringent controls. Photonic devices on chips are increasingly being demonstrated for chemical and biological sensing with performance metrics rivaling benchtop instruments and thus promising the potential of portable, handheld, and wearable monitoring of various chemical and biological analytes. In this paper, we review recent advances in MIR silicon photonics research. We discuss the pros and cons of various platforms, the fabrication procedures for building such platforms, and the benchmarks demonstrated so far, together with their applications. Novel device architectures and improved fabrication techniques have paved a viable way for realizing low-cost, high-density, multi-function integrated devices in the MIR. These advances are expected to benefit several application domains in the years to come, including communication networks, sensing, and nonlinear systems.

OCIS codes: (130.3120) Integrated optics devices; (230.7370) Waveguides; (130.3060) Infrared; (250.5300) Photonic integrated circuits.

https://doi.org/10.1364/PRJ.6.000254

1. INTRODUCTION

The mid-infrared (MIR) region, typically defined as wavelengths from 2 to 20 μm, has potential for many applications including absorption spectroscopy, thermal imaging, and free-space communication. Of these, trace gas detection based on molecular absorption spectroscopy is of great interest for various sensing applications in civilian and military domains. It is well known that the MIR range is called a "molecular fingerprints" region due to the presence of fundamental vibration signatures of almost all chemical bonds [1] in this wavelength range. In particular, the $\lambda = 3$–5 μm and $\lambda = 8$–12 μm wavelength regions are significant due to the presence of atmospheric transmission windows in these bands. Absorption-spectroscopy-based detection has an overwhelming advantage over other methods that depend on sensing changes in refractive index that lack specificity to identify the exact analyte. In absorption spectroscopy, by detecting the optical attenuation as light passes through the analytes at their specific absorbance wavelengths, the analyte composition can be determined qualitatively and quantitatively. Although overtones of molecular vibration signatures extend into the near-infrared (NIR) and visible wavelength domains ($\lambda < 2$ μm) that can also be detected by well-developed absorption spectroscopy techniques, fundamental chemical absorption cross sections are orders of magnitude larger in the MIR than in the NIR and visible, so by moving from NIR to MIR, the sensitivity of detection can be enhanced by several orders. In recent years, the prospect of complete lab-on-chip MIR absorption spectrometers has been enhanced by the advent of room-temperature, high-power, and tunable quantum cascade lasers (QCLs) [2] and interband cascade lasers (ICLs). However, in addition to the need of a separate off-chip multi-pass gas cell, the sensing methods rely on elaborate and fragile optical alignment between the light source, the detector, and the gas cell. The popular techniques for absorption spectroscopy include Fourier transform infrared spectroscopy (FTIR) [3], tunable direct laser absorption spectroscopy (TDLAS) [4], cavity ring-down spectroscopy

(CRDS) [5], and photo-acoustic spectroscopy (PAS) [6]. To date, all commercial systems are bulky and expensive. Methods such as CRDS require high-finesse optical mirrors that are typically expensive to manufacture and are typically restricted in the MIR by the lack of appropriate materials that can be polished to the same finesse using current engineering technology. A portable/handheld on-chip, low size, weight, and power (SWaP) integrated MIR absorption-spectroscopy-based sensor, with a chip-integrated light source, detector, and absorbance transducer is highly desired and is one of the driving forces for MIR research.

Recently, driven by the accelerating increase of the volume of data traffic, the originally considered effectively infinite bandwidth of the NIR spectrum gradually faces the so-called "capacity crunch" challenge. To keep pace with increasing demand, new modulation techniques or new spectral regions that can increase the bandwidth capacity are urgently demanded. The MIR region offers such a new spectrum for bandwidth extension since two atmospheric transmission windows (3–5 μm and 8–12 μm) are within this region. Building on-chip transceivers in the MIR opens new spectra for addressing steep growth in the volume of data transmitted over optical networks. Although the future in MIR-integrated photonics is very bright, the biggest challenge is the lack of an appropriate MIR transparent or low-loss optical core and cladding material. Currently, MIR waveguides are fabricated from a limited set of transparent materials like chalcogenide glasses [7–9], silver halide [10–12], silicon nitride [13–15], III–V [16–18], aluminum nitride [19], mercury–cadmium–telluride (MCT) [20], silicon carbide [21], germanium [22–28], silicon germanium [29–32], etc. It is worth mentioning that some of the aforementioned results are grown on silicon substrates, such as germanium and silicon germanium, which are within the scope of silicon photonics. However, in this paper, we only focus on platforms using silicon as the guiding material.

Silicon photonics is seen as a promising platform for future integrated devices, benefiting from its low material losses, mature fabrication technology, and high refractive index. So far, most of the research in silicon photonics has been at telecom wavelengths, and many breakthroughs have been achieved in optical interconnect or optical sensing applications. As proposed by Soref [33], silicon is not only an idea platform for NIR, but also for MIR, since it has a wide optical transparent window from 1.1 to 8 μm. Compared to NIR, MIR silicon photonics at present is still somewhat in infancy. However, the high refractive index of silicon ensures high-density integration, and the CMOS compatibility enables low-cost, high-volume manufacturing. Furthermore, since the two-photon absorption effect becomes negligible in the MIR, it has potential for nonlinearity-based broadband light source generation. All these attributes make MIR silicon photonics very attractive. Silicon-on-insulator (SOI) is widely used in the NIR silicon photonics community. However, the buried oxide layer has strong absorption loss in the range between $\lambda = 2.6$–2.9 μm and $\lambda > 3.6$ μm that limits the application range of such wafers. To address this issue and fully exploit the transparent window of silicon on SOI, free-standing structures have been proposed and experimentally demonstrated, such as suspended-membrane silicon rib [34] and subwavelength grating (SWG) waveguides [35], to potentially extend the application capability to $\lambda = 8$ μm, however, such devices impose design constraints, fabrication complexities, and have the potential to be fragile in harsh sensing environments. Hence, a silicon-on-sapphire (SOS) platform was proposed as an alternative platform. SOS has a transparent window up to $\lambda = 5.5$ μm as well as high refractive index contrast $\Delta n \sim 1.7$ between the core and the undercladding sapphire. Other than the two above-mentioned platforms, several other platforms have been proposed and demonstrated in the MIR, showing different pros and cons.

In this paper, we aim to provide an overview of recent progress in MIR silicon photonics. We will review most silicon platforms, including SOI, SOS, standard silicon wafer, silicon-on-nitride (SON), silicon-on-calcium-fluoride (SOCF), as well as silicon-on-lithium-niobate (SOLN). The design, fabrication, and results of the basic building blocks on each platform will be discussed. The paper is organized based on platform category as follows: devices on SOI, including SOI without undercut and free-standing structures built on SOI, are discussed in Section 2. In Section 3, we discuss devices on SOS platform, covering the basic building blocks as well as the applications in optical sensing, optical communications, and nonlinear applications. In Section 4, we provide brief details on devices built on standard silicon wafer with special design and fabrication processes. Other new platforms, such as SON, SOCF, and SOLN are presented in Section 5, and the paper concludes with our vision of the future of MIR silicon photonics in Section 6.

2. SILICON-ON-INSULATOR

SOI is the most prevalent material platform for building silicon devices operating in the NIR region. However, due to strong absorption of the buried oxide in the range between 2.6 and 2.9 μm and beyond 3.6 μm [33], all devices demonstrated so far on SOI platforms without undercutting are at wavelengths below 4 μm, and they focus on the applications that do not need to operate at the opaque region of SiO_2, such as optical communications [36–38], on-chip spectrometers [39–41], and nonlinear applications [42–51]. Also, since the developments on this platform in MIR are relatively more mature compared with other platforms, several review papers are available [15,52–56]; we thus briefly go through several important achievements on the SOI platform.

A. Devices on SOI Platforms without Undercut

1. Passive Devices on SOI Platforms Operating in Short-Wave Infrared

At telecommunication wavelengths and short-wave infrared (SWIR, 2–2.5 μm), SOI wafers with a 220-nm-thick silicon layer represent the standard thickness. Several basic passive optical components have been demonstrated using SOI with a 220-nm silicon layer, including high-efficiency grating couplers [57], low-loss single-mode waveguides [57], concave gratings (also known as echelle grating) [40], arrayed waveguide gratings (AWG) [40], as well as ring resonators [58].

In 2012, Hattasan *et al.* demonstrated high-efficiency grating couplers and low-loss single-mode waveguides for transverse-electric (TE)-polarized light on an SOI wafer with a 220-nm-thick silicon layer operating in the SWIR region

[57]. The grating coupler consists of a 220-nm-thick crystalline silicon layer as a waveguide layer with a 160-nm poly-silicon overlay on top of the waveguide. The fabricated grating coupler [Figs. 1(a) and 1(b)] showed −3.8 dB coupling efficiency from a standard single-mode fiber to an SOI waveguide at $\lambda = 2.1$ μm. Single-mode waveguides, 900 nm wide and 220 nm high, were characterized, showing 0.6 dB/cm in SWIR [Fig. 1(c)].

SOI-based spectrometer platforms for wide-band spectroscopy from 1510 to 2300 nm were reported by Ryckeboer *et al.* in 2013 [40]. Two types of spectrometers, planar concave gratings (PCGs, also known as echelle grating) and AWGs, were demonstrated in the SWIR region [Fig. 1(d)]. A high-resolution (100 GHz or 1.6 nm) AWG for TE-polarized light with a central wavelength of 2.2 μm, insertion loss of 4 dB, crosstalk of −16 dB, and a footprint about 1 mm^2 was demonstrated. In the meantime, a low-resolution (300 GHz or 4.8 nm) AWG using 0.48 mm^2 area for the same polarization and same central wavelength was reported, showing an insertion loss of 2.15 dB and a crosstalk of −12 dB. Both demonstrated AWGs had 36 arrayed waveguides and showed high performance at $\lambda = 2$–2.25 μm. Four PCGs with different parameters were demonstrated in the same paper with a low crosstalk −16 dB for all PCGs.

A ring resonator with a 350-μm circumference, 450-nm coupling gap, and 20-μm coupling length was demonstrated by Leo *et al.*, showing a loaded Q of 75,000 [Fig. 1(e)] [58].

Very recently, Rouifed *et al.* reported an ultra-compact multimode interference (MMI)-based wavelength demultiplexer at $\lambda = 2$ μm [59]. The devices were based on shallow-etch rib waveguides on a 340-nm SOI platform with a footprint of 293×6 $μm^2$. Low insertion loss of 1.2 dB at 2 μm with contrast ∼20 dB and a crosstalk of 18.83 dB was observed.

The SWIR region is still within the transparent window of SiO_2, so passive devices reported in this regime are very similar to devices in the NIR, requiring no special fabrication processes. Even the 220-nm thickness is enough for most devices operating in this region. In the meantime, the absence of two-photon absorption provides more benefits. Therefore, the SOI platform is an ideal platform for the development of nonlinear applications that may find great value in future MIR optical communications and signal-processing applications.

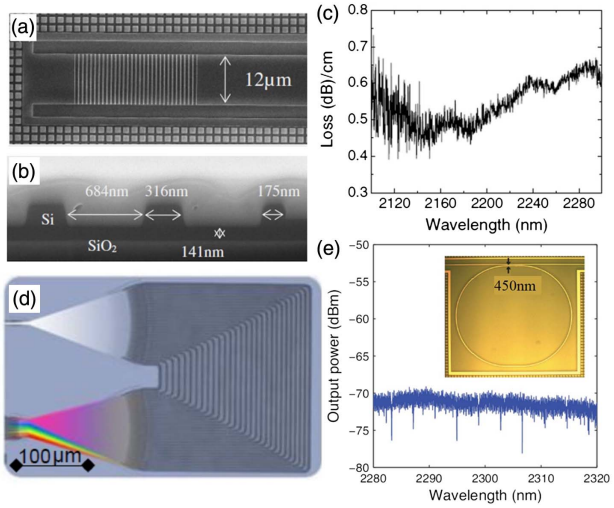

Fig. 1. Passive devices on an SOI platform for SWIR. (a) and (b) Top view and cross section of scanning electron microscope (SEM) images of the fabricated SWIR grating couplers [57]. (c) SOI single-mode waveguide propagation loss in the SWIR [57]. (d) Microscope image of an AWG [40]. (e) Transmission spectrum of a ring resonator (inset) in wavelength range between 2.28 and 2.32 μm [58]. Figures are reproduced from: (a)–(c) Ref. [57]; (d) Ref. [40]; (e) Ref. [58].

2. Passive Devices on SOI Platforms beyond SWIR

As the operating wavelength increases, a thicker silicon layer and a thicker bottom oxide are required to prevent substrate leakage. Mashanovich *et al.*, in 2011, reported a propagation loss as low as 0.6–0.7 dB/cm at 3.39 μm for both TE and transverse magnetic (TM) polarization using 2-μm-thick rib waveguides on SOI [60]. The bottom oxide needs to be at least 2 μm to suppress substrate leakage, which was confirmed by comparison between waveguides with different bottom oxide thicknesses [60]. Later, rib waveguides with the same geometry as in Ref. [60] were tested at wavelengths of 3.73 μm and 3.8 μm for TE polarization, showing 1.5 ± 0.2 dB/cm and 1.8 ± 0.2 dB/cm propagation loss, respectively [61]. The authors also measured strip waveguides [Fig. 2(a)] of 500 nm high and 1000 nm tall with TE polarization at 3.74 μm, showing propagation loss of 4.6 ± 1.1 dB/cm. A strip-waveguide-based 1×2 MMI power splitter [Fig. 2(b)] and racetrack resonators [Fig. 2(c)] were characterized too, providing 3.6 ± 0.2 dB/MMI and Q of 8200 at 3.74 μm for the racetrack resonator [61]. Increased silicon layer thickness by adding poly-silicon on top of the original 220-nm SOI [Fig. 2(d)] was reported [39]. The results were shown about 5.8 dB/cm at 3.8 μm. Crystalline silicon strip waveguides 400 nm in width and 1350 nm in height had a better performance, providing 3.1 dB/cm at 3.8 μm [39]. A reduction of propagation loss to 1.46 ± 0.2 dB/cm for 400-nm rib SOI waveguides with 220-nm etch depth at 3.77 μm was reported by Nedeljkovic *et al.* [55]. Recently, the same group further improved the

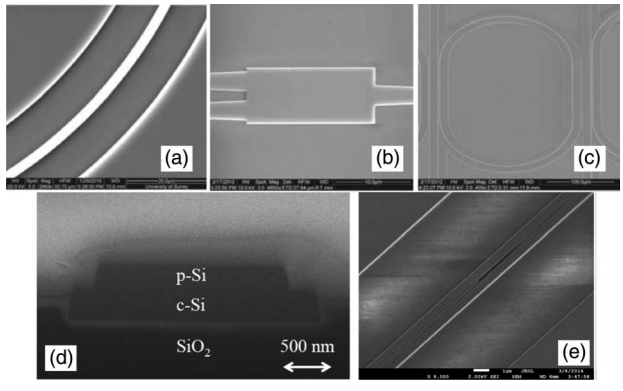

Fig. 2. Passive devices on SOI with a thicker silicon layer. SEM images of strip-waveguide-based (a) bending [61]; (b) MMI device [61]; (c) racetrack resonator [61]. (d) SEM cross section image of a waveguide implemented in the imecAP process where the thickness of the p-Si layer is 160 nm and the thickness of c-Si is 220 nm [39]. (e) SEM image of the mode converter between a strip waveguide and a slot waveguide [62]. Figures are reproduced from: (a)–(c) Ref. [61]; (d) Ref. [39]; (e) Ref. [62].

waveguide performance, showing 1.28 ± 0.65 dB/cm propagation loss at 3.77 μm using strip waveguides 500 nm in height and 1.3 μm in width [54]. It is noted that the propagation loss of strip waveguide is significantly larger than that of a rib waveguide due to more interactions with etch-induced side-wall roughness. But better optical confinement of strip waveguide leads to smaller bending radius and potential higher integration density. Very recently, Dong *et al.* reported the SOI channel waveguides with propagation loss around 2 dB/cm and bending loss, for a 10-μm bending radius, about 0.02 dB/90° in the wavelength range of 3.68–3.88 μm [63]. Hu *et al.* have also shown low-loss MIR silicon waveguides on a SOI platform with propagation loss about 2.65 ± 0.08 dB/cm for a strip waveguide at 3.7 μm, 1.75 ± 0.22 dB/cm for a rib waveguide at 3.75 μm, bending loss of about 0.054 dB/90° for a 5-μm bending radius, and about 0.008 dB/90° for a 25-μm bending radius [15]. The low propagation loss and bending loss promoted the realization of strip and rib directional couplers, showing 50% power splitting ratio at the coupling lengths of 21 μm and 8 μm, respectively [15]. The strip racetrack resonators with Q factor of 5900, extinction ratio (ER) of 6.84, and free spectral range (FSR) of 85 nm were also reported [15]. These results indicate that the absorption loss of SiO_2 can still be tolerable at longer wavelengths if the waveguide is designed and fabricated properly. So far, SOI-based waveguides operating beyond a 4-μm wavelength without undercut have not yet been reported, but we expect that better cross-section engineering on a thicker silicon layer will minimize the mode overlap with the bottom oxide and push the working range to even longer wavelengths.

Chip-based sensing methods benefit from high optical interaction between the optical mode and the analyte. Various methods to increase the optical mode overlap integral with the analyte have been experimentally demonstrated using slot waveguides. Recent research has shown the enhancement can go up to 50 times higher compared to conventional waveguides [64]. The first SOI-based MIR slot waveguide was demonstrated by Nedeljkovic *et al.* with 9 dB/cm propagation loss at 3.8 μm [55]. The waveguides were partially etched. The mode converter [Fig. 2(e)] had a transition loss of about 0.04 dB/interface. Later, the same group improved the propagation loss of fully etched slot waveguides to 2.6 ± 0.24 dB/cm at 3.8 μm [54]. The latest results from them show 1.4 ± 0.2 dB/cm propagation loss for fully etched slot waveguides with height of 500 nm, silicon width of 650 nm, and slot gap of 78 nm at 3.8 μm. The authors demonstrated strip-to-slot transition loss of 0.09 ± 0.01 dB/transition and slot bending loss of 0.18 dB/bend [62]. The significant progress greatly releases the constraint of integration length and steps forward towards the real applications.

Improving fabrication also led to significant reduction in MMI insertion loss to 0.10 ± 0.01 dB at 3.8 μm [55], which was much lower than previously reported results in the MIR [61,65]. Such loss reduction, especially the propagation loss and insertion loss, lays a solid base for implementation of MIR photonic integrated circuits (PICs) in silicon.

New MIR SOI devices with special functionalities have been demonstrated. The AWGs and PCGs shown in previous subsection operating in SWIR were fabricated and tested at 3.8 μm using a thicker silicon layer, achieving low insertion loss (1.5–2.5 dB) and low crosstalk (15–20 dB) [39]. The performance improvements of MMI facilitate the Mach–Zehnder interferometer (MZI), which includes MMIs as power splitters and combiners. A MIR-slot-waveguide-based MZI was also reported [55]. At the same time, an angled MMI (AMMI)-based three-channel multiplexer with insertion losses around 4–5 dB and crosstalk of −12 dB was demonstrated, providing an alternative approach for wavelength division (de)multiplexing, which is important for MIR communication integrated circuits and sensors [55].

MIR absorption spectroscopy is highly relevant to a lot of sensing applications. FTIR spectroscopy is an important technique to characterize the absorption signatures. Thus, integrating this technique onto a chip, building an on-chip FTIR will have a broad impact in the scientific community. Recently, Nedeljkovic *et al.* demonstrated the first MIR Fourier-transform (FT) SOI spectrometer chip [41]. The device was based on the principle of spatial heterodyne spectroscopy in a planar waveguide configuration [66]. The spectrometer consists of an array of 42 MZIs with linearly increasing optical path length differences, generating a stationary interferogram from which the input spectrum is recovered with FT-based techniques. Two types of spectrometers, conventional asymmetric-MZIs-based [Fig. 3(a)] and spiral-arm-MZIs-based, were used to implement this function. The results show that a spectral resolution below 3 nm can be achieved from both types of spectrometers.

Similar to ring resonators, racetrack resonators can provide high-resonance Q and are thus very important for optical sensing and signal processing. The Vernier effect is well known as an efficient method for performance improvment, such as sensitivity amplification. Using cascade-coupled racetrack resonators [Fig. 3(b)], the Vernier effect was experimentally demonstrated by Troia *et al.* in the MIR range of 3.7–3.8 μm [67]. The insertion loss was lower than 1 dB, and had a maximum interstitial peak suppression of 10 dB.

Based on the AMMI mentioned above, Hu *et al.* interleaved the AMMIs and implemented a wavelength division (de)multiplexing device in MIR on a SOI platform [68]. The device was based on rib waveguides and consisted of an asymmetric MZI and two AMMIs [Figs. 3(c) and 3(d)]. Compared to previous work, which used a single AMMI, the channel count was doubled and channel spacing halved with almost the same

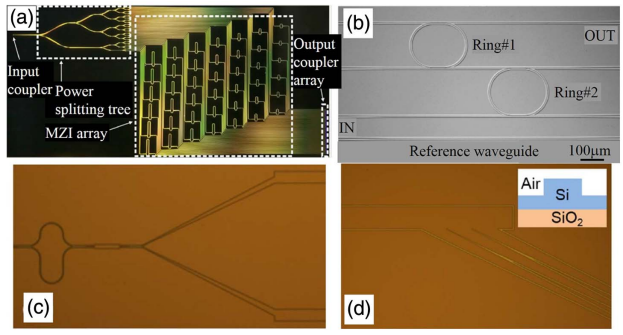

Fig. 3. Other passive devices on SOI operating beyond SWIR. Optical microscopy images of (a) FTIR spectrometer with conventional asymmetric MZIs [41]; (b) the Vernier architecture [67]; (c) fabricated MZI and the AMMIs' inputs [68]; (d) output of IAMMI. The inset shows the cross section of the waveguides [68]. Figures are reproduced from: (a) Ref. [41]; (b) Ref. [67]; (c) and (d) Ref. [68].

insertion loss and a slight increase of device footprint. An insertion loss of 3–4 dB and a crosstalk of 15–18 dB were achieved.

3. Active Devices on an SOI Platform

As noted earlier, the huge volume of data transmitted over optical networks consumes most part of the traditional telecommunication bandwidth. A promising solution is to find out new spectral regions for optical communications. Following this trend, considering the potential bandwidth in MIR, it makes sense to investigate MIR active devices for optical communication applications. In 2012, Van Camp *et al.* demonstrated the first MIR electro-optic (EO) modulator in SOI at 2165 nm [37]. The modulator was a free-carrier injection-based silicon MZI modulator [Fig. 4(a)]. It consisted of rib-waveguide-based asymmetric MZI, thermo-optic (TO) heaters for bias point control, as well as radio frequency (RF) signal inputs. The modulator had a $V\pi \cdot L$ figure of merit of 0.12 V · mm and extinction ratio of −23 dB. The modulation speed can go up to 3 Gbit/s [37]. An MIR TO modulator has also been reported [36]. Using spiral-based asymmetric MZI, placing aluminum heaters on one MZI arm [Figs. 4(b) and 4(c)], the modulators operating at 3.8 μm with a 30.5-dB-high modulation depth, and −3 dB bandwidth at 23.8 kHz were demonstrated. The switching power was around 47 mW [36]. The speed of the TO modulator may however be more suitable for some low-speed switch applications or acting as an on-chip chopper for integrated spectrometers rather than being a modulator.

Silicon is not a good material for building lasers due to its indirect band gap. One potential approach to solve the light source issue in MIR silicon platform is bonding a III-V laser onto a silicon waveguide. In 2013, Dong *et al.* demonstrated

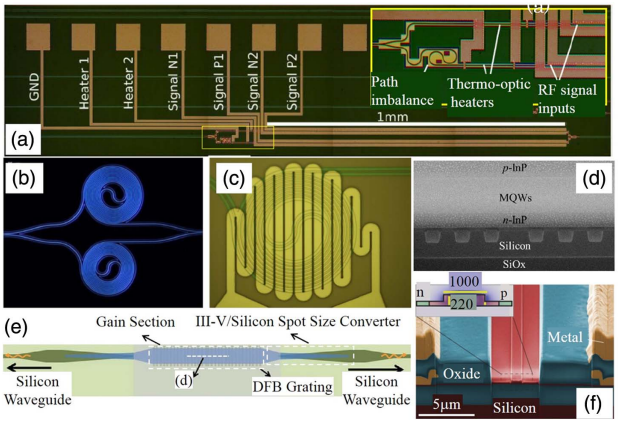

Fig. 4. Active devices on an SOI platform. (a) Optical microscope image of the asymmetric MZI modulator. Inset: magnified detail of the 50/50 Y-junction, optical path imbalance, thermo-optic heaters, and RF signal inputs [37]. (b) Optical microscope images of a spiral-arm asymmetric MZI [36]. (c) Aluminum heater sits on top of one arm of the spiral MZI [36]. (d) SEM image of the longitudinal cross section of the gain region shown in Fig. 4(e) [69]. (e) Schematic of the III-V-on-silicon DFB laser [69]. (f) Cross section view of the photodetector shown in false color to distinguish the materials. Inset shows schematic of the silicon waveguide with dimensions labeled in nanometers, and with TE mode at 2 μm overlaid [38]. Figures are reproduced from: (a) Ref. [37]; (b) and (c) Ref. [36]; (d) and (e) Ref. [69]; (f) Ref. [38].

an electrically pumped pulsed, room-temperature, hybrid III-V/silicon laser at the wavelength of 1.9 μm using the wafer-bonding technique [70]. Even though the wavelength is slightly shorter than 2 μm, it provides an example for integrating semiconductor lasers on silicon in the MIR. After that, Roelkens *et al.* reported a preliminary result of a Fabry–Perot GaSb-on-silicon hybrid laser using adhesive wafer bonding at 2.38 μm wavelength under pulsed operation at 10°C [71]. In 2015, Spott *et al.* heterogeneously integrated III–V/silicon lasers using strained InGaAs type-I heterostructures and demonstrated a room-temperature continuous-wave (CW) laser, emitting power up to 4.2 mW from a single-face, at 2 μm wavelength [72]. Besides the aforementioned devices, heterogeneous integration of InP-based type-II quantum-well Fabry–Perot lasers [73] and distributed feedback (DFB) lasers [Figs. 4(d) and 4(e)] [74], both emitting at 2.3 μm wavelength under CW operation at 5°C with silicon waveguides have been reported by Wang *et al.* Recently, the same group also demonstrated a hybrid III-V/silicon DFB laser array spanning from 2.28 to 2.43 μm wavelengths with CW operation close to room temperature [69]. This is an important step towards an on-chip integrated silicon spectroscopic sensing system.

Similar to bonding III-V lasers onto silicon waveguides, bonding III-V detectors onto silicon waveguides is a candidate for monolithic detectors in the MIR. Several devices, such as heterogeneously integrating p-i-n photodetectors on top of the PCGs for spectroscopy [40], integrating with AWG for on-chip laser monitoring [75], and heterogeneously integrating InP-based type-II quantum-well photodiodes for operation in the 2.2–2.4 μm wavelength range [76] have been reported. On the other hand, even though silicon is transparent starting at 1.1 μm, it can act as a photodetector if mid-bandgap states are created, which can be realized through ion implantation. Ion-implanted MIR silicon photodetectors were demonstrated by Ackert *et al.* in 2015, at 1.96 μm with a bit rate of 20 Gbit/s [38]. An SOI rib waveguide was implanted with boron to form a p-i-n photodiode [Fig. 4(f)] operating in the avalanche regime for high-speed detection, showing the external responsivity of the detector at 2.02 μm is 0.3 ± 0.02 A/W. The easy fabrication as well as CMOS compatibility makes such photodetectors very promising for optical communications beyond traditional telecommunication windows.

4. Devices on SOI Platforms for Nonlinear Applications

Silicon photonics is not only a good platform for linear integrated photonic circuit implementation, but also can be a very good platform for exploring nonlinear effects due to the tight confinement of guiding light, significantly enhancing the light intensity. Especially in the MIR, two-photon absorption and associated free-carrier absorption are substantially reduced at wavelengths beyond 2.2 μm, making it ideal for implementation of nonlinear optical functions. Liu *et al.* exploited efficient four-wave mixing in 2-cm-long silicon strip waveguides, 220 nm in height and 900 nm in width, to facilitate spectral translation of a signal at 2440 nm to the telecom band at 1620 nm across a span of 62 THz [Figs. 5(a) and 5(b)] [44]. A simultaneous parametric translation gain of 19 dB was observed, which can significantly boost sensitivity to weak MIR signals. This demonstration promises the potential of

generating and detecting MIR signals based on mature NIR sources and detectors, respectively.

An SOI ring-resonator–based [Fig. 5(c)] on-chip frequency comb spanning from 2.1 to 3.5 μm with frequency spacing about 127 GHz [Fig. 5(d)] was demonstrated by Griffith *et al.* [43]. The ring resonator was fabricated using an etchless process, showing a loaded Q about 220,000, and the intrinsic Q is 590,000. To eliminate silicon's nonlinear loss, the ring resonator was also doped to form a PIN junction that, in a reverse bias, carriers generated from three-photon absorption will be swept out of. A frequency comb was generated with 150 mW of input optical power, under a 10-V reverse bias applied on the PIN junction. The demonstrated device was compact, robust, and had a relatively easy fabrication process. Therefore, it may offer a great potential for field applications.

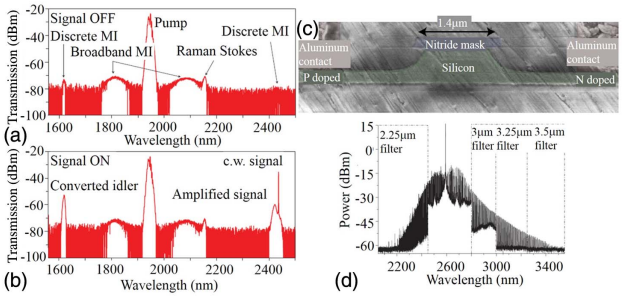

Fig. 5. Nonlinear response on an SOI platform. Output transmission spectrum with pump operating at 1946 nm when the input signal is (a) off, (b) on. Parametric amplification of the signal occurs, with simultaneous spectral translation across 62 THz, to an idler at 1620 nm [44]. (c) SEM image of cross section of the etchless silicon microresonator with integrated PIN diode, shown in false colors [43]. (d) MIR broadband frequency comb generation from 2.1 to 3.5 μm in the etchless silicon microresonator [43]. Figures are reproduced from: (a) and (b) Ref. [44]; (c) and (d) Ref. [43].

Besides the above two demonstrations, several applications exploiting nonlinear effects have been demonstrated in the SOI platform in MIR, such as electric-field-induced second-order nonlinearity for second harmonic generation (SHG) [47,48], supercontinuum generation (SCG) spanning from 1.5 to 3.6 μm [49], optical parametric amplifiers (OPAs) with broadband gain as high as 25.4 dB from 2060 to 2280 nm [46], etc.

A summary for this section, covering SWIR and MIR (<4 μm), is given in Table 1. The SOI platform thus shows significant promise for various applications to $\lambda \sim 4$ μm in MIR.

B. Free-Standing Devices in SOI

1. Suspended-Membrane-Based Devices

As mentioned in Section 1, SiO_2 is highly absorptive in the range between $\lambda \sim 2.6$ and 2.9 μm and above $\lambda = 3.6$ μm. Therefore, due to the loss from SiO_2 underneath, a traditional SOI platform is not suitable for wavelengths longer than $\lambda = 4$ μm. In order to fully utilize the transparency region of silicon on an SOI platform, the buried oxide layer must be removed, leaving a suspended silicon membrane. The first experimental demonstration of such devices came from Cheng *et al.* in 2012 [77,78]. While the suspended hole-type photonic crystals (PCs) have been demonstrated often in the NIR [79,80], which inherently have two connecting membranes, suspended-membrane (SM)-based waveguides require a certain thickness of residual slab to connect the two banks. The conventional strip waveguides do not work at this condition. Therefore, for SM-based waveguides, two etch steps are

Table 1. Devices and Applications on an SOI Platform

Category	Representative Device Performance
Waveguides [15,39,54,55,57,60,61,63]	Propagation loss: 0.6 dB/cm for TE at $\lambda = 2.1$ μm [57]; 0.6–0.7 dB/cm for both TE and TM at $\lambda = 3.39$ μm [60]; 1.5 dB/cm for TE around $\lambda \sim 3.73$ μm [61]; 1.28 dB/cm for TE at $\lambda \sim 3.8$ μm [54]
Slot waveguides [54,55,62]	Propagation loss: 1.4 dB/cm at $\lambda = 3.8$ μm [62]; 0.18 dB/bend [62]; mode conversion: 0.09 dB/transition [62]
Grating couplers [41,57]	Coupling efficiency: −3.8 dB for TE mode at $\lambda = 2.1$ μm [57]; N/A for SWG working at $\lambda \sim 3.8$ μm [41]
Resonators [15,43,58,61]	Q: 75,000 at $\lambda \sim 2.3$ μm [58]; 8200 at $\lambda = 3.74$ μm [61]; loaded $Q \sim 220,000$, intrinsic $Q \sim 590,000$ [43]
MMI [55,59,61]	Insertion loss: 1.2 dB at $\lambda = 2$ μm [59]; 0.1 dB around $\lambda = 3.8$ μm [55]
Directional coupler [15]	Strip- and rib-waveguide-based, 50% power split ratio [15]
Passive applications [40,41,67,68]	AWG at $\lambda = 2.2$ μm : 1.6 nm resolution for TE, 4 dB insertion loss, −16 dB crosstalk, and 1 mm^2 footprint [40]; 4.8 nm resolution for TE, 2.15 dB insertion loss, −12 dB crosstalk, and 0.48 mm^2 footprint [40]. PCG at $\lambda = 2.2$ μm : −5 dB insertion loss, −16 dB crosstalk [40]; FT spectrometer: consisting of 42 MZIs, 2.7 nm resolution, 57 nm FSR [41]; Vernier effect at $\lambda = 3.7$–3.8 μm: 1 dB insertion loss, 10 dB interstitial peak suppression [67]; WDM at $\lambda = 3.7$–3.8 μm: 3–4 dB insertion loss and 15–18 dB crosstalk [68]
Modulators [36,37]	EO modulator at $\lambda = 2165$ nm: $V\pi \cdot L = 0.12$ V · mm, ER: 23 dB; modulation speed of 3 Gbit/s [37]; TO modulator at 3.8 μm: 30.5 dB modulation depth, 23.8 kHz bandwidth; 47 mW switching power [36]
Light source [69–74]	FP laser: at 2 μm, CW mode at room temperature, 4.2 mW [72]; at 2.3 μm, CW mode at 5°C, 1.3 mW [73]; DFB laser: at 2.32 μm, CW mode ~17°C, suppression ratio of 40 dB at 10°C and with 190 mA bias current [74]; DFB laser array: spanning 2.28–2.43 μm, at 2.35 μm CW mode up to 25°C, 2.7 mW in a single mode at 5°C [69]
Detectors [38,40,75,76]	At ~2 μm, bit rate: 20 Gbit/s; external responsivity: 0.3 A/W [38]; responsivity of 1.2 A/W at $\lambda = 2.32$ μm and 0.6 A/W at $\lambda = 2.4$ μm [76]
Devices for nonlinear applications [42–51]	Frequency comb spanning from $\lambda = 2.1$ to 3.5 μm, frequency spacing 127 GHz [43]; spectral translation 62 THz (from $\lambda = 2440$–1620 nm), 19 dB parametric translation gain [44]; OPA: 220 nm gain bandwidth as high as 25.4 dB [46]; maximum SHG efficiency 13% ± 0.5% W^{-1} at $\lambda = 2.29$ μm [48]; SCG from $\lambda = 1.5$ to 3.6 μm [49]

required. The first one is to form the rib waveguide, and the second is to puncture holes in the silicon slab for removing the buried oxide. Cheng *et al.* demonstrated several SM-based devices at $\lambda = 2.75$ μm [Figs. 6(a)–6(d)], including a focusing subwavelength grating coupler [77], a rib waveguide [77], and a racetrack resonator [78]. All of the devices were started from SOI with 340-nm-thick silicon membrane. The residual slab was 100 nm thick, and the waveguides were 1000 nm wide. The holes were placed approximately 3 μm from the rib waveguides so as not to disturb the mode propagation. The efficiency of subwavelength grating coupler was 24.7% for the TE mode, and the propagation loss was 3.0 ± 0.7 dB/cm for TE-polarized light. Bending loss for a radius larger than 40 μm was negligible. The thermal tuning method was employed to measure the SM-based racetrack resonator (bending radius about 250 μm, coupling length about 40 μm, and coupling gap 600 nm) showing $Q \sim 8100$. By placing a monolayer graphene on such waveguide, a photodetector with a fast responsivity

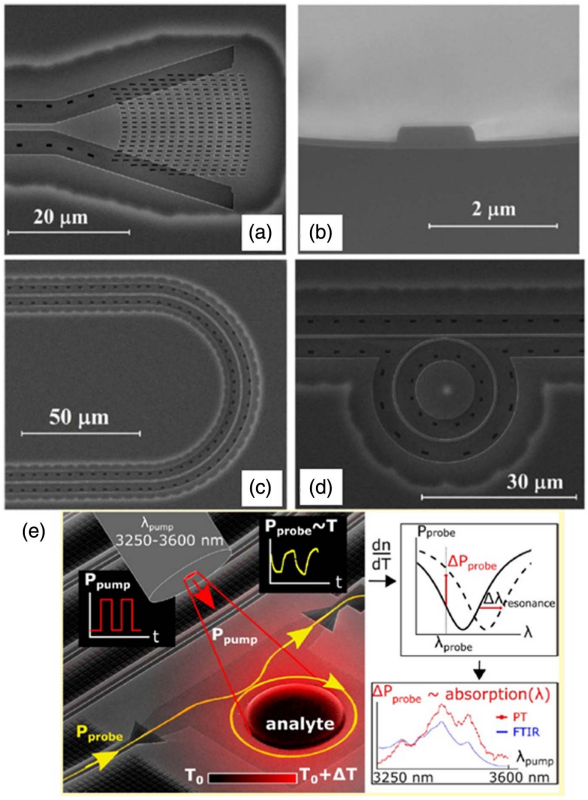

Fig. 6. Suspended-membrane-based devices on an SOI platform. (a)–(d) SEM images of suspended devices in SOI: (a) focusing SWG coupler; (b) SM waveguide cross section with etch depth ~240 nm, residual slab thickness ~100 nm, and width ~1 μm; (c) straight and bending SM waveguide with bending radius ~40 μm; (d) SM-based ring resonator with radius ~10 μm [78]. (e) SM-based ring resonator for MIR photothermal spectroscopy. Heat generated through absorption of the MIR pump beam increases the temperature of the suspended ring resonator and then shifts the resonance wavelength induced by the thermo-optic effect. It leads to a change in the output power of the fixed-wavelength NIR probe light. The absorption spectrum of the analyte can be reconstructed through pumping wavelength scanning [81]. Figures are reproduced from: (a)–(d) Ref. [78]; (e) Ref. [81].

~0.13 A/W at a 1.5 V bias working at $\lambda = 2.75$ μm was demonstrated [82]. SM-based rib waveguides and ring resonators were also reported by Xia *et al.* in 2013, with $Q \sim 2700$ at $\lambda = 5.2$ μm and $Q \sim 7900$ at $\lambda = 3.4$ μm [83]. A recent paper from Miller *et al.* showed improved Q of SM-based ring resonators to 83,000 at $\lambda = 3.79$ μm using an etchless process together with a demonstration of inverse nanotaper for light coupling [84].

An interesting work from Vasiliev *et al.* was reported recently, using SM-based ring resonators to transduce the generated heat through optical absorption to NIR output power variations for on-chip MIR photothermal spectroscopy [81]. The ring resonator was probed by an NIR tunable laser while it was pumped by an MIR source (3250–3600 nm) [Fig. 6(e)]. Photoresist AZ5214 as a representative of analytes was patterned in the annular region. When the pumping wavelengths match the absorption peaks of the photoresist, the light will be absorbed by the photoresist and heat will be generated, which in turn increases the temperature of the ring resonator. The TO effect will transfer the temperature change to the effective index variations inside the ring, leading to the resonance peaks' shift. By sweeping the pumping wavelengths and decoding the output NIR probing power, the absorbance of the testing analytes will be reconstructed. It is noted that the free-standing structure provides better thermal isolation and increases the signal by a factor of 40. Also, this is a good way to circumvent the need for bulky and expensive MIR detectors by using a cheaper NIR readout system.

Since their conceptual inception through the theoretical studies of Yablonovitch [85] and John [86], PCs have generated significant interest in the scientific community due to their ability to guide and trap light in length scales of the wavelength of light. PC cavities [87,88] and PC waveguides (PCWs) [89] have been demonstrated in SM in SOI. The first MIR PC structure in SOI was demonstrated by Shankar *et al.* in 2011 [88]. The PC structure they investigated was an SM-based L3-type PC cavity, which had three missing holes inside a hexagonal lattice structure on an SOI platform with operating wavelength $\lambda = 4.4$ μm [Figs. 7(a)–7(c)]. The authors developed a "scanning resonant scattering microscopy" method to image the cavity modes. A resonance with $Q \sim 13,600$ was experimentally observed [88]. They also reported observation of optical bi-stability in PC cavities working around $\lambda = 4.5$ μm [87]. This phenomenon is due to the thermal effect with a time constant on the order of 5 μs. After annealing in a N_2 environment, this phenomenon disappeared. A surface treatment (piranha/HF cycles and annealing) was developed, showing improved Q from 11,500 to 29,300, and the best measured Q was around 45,000 at $\lambda = 4.48$ μm.

In 2012, Reimer *et al.* demonstrated a PCW in silicon SM with guiding region in the wavelength range of $\lambda = 2.9$–3.9 μm [89]. The PCW investigated was a standard W1 PCW with a hexagonal lattice of air holes, which indicates missing a row of holes along the $\Gamma - K$ direction. The devices were fabricated in a 500-nm-thick SM with lattice constant (a) between $\lambda = 1040 - 1120$ nm, and hole radii $r = 0.26\,a - 0.28\,a$ [Fig. 7(d)]. The measurement results clearly showed the onset of guiding region, the light line position, and the PC bandgap [Fig. 7(e)]. By integrating an unbalanced MZI onto the chip

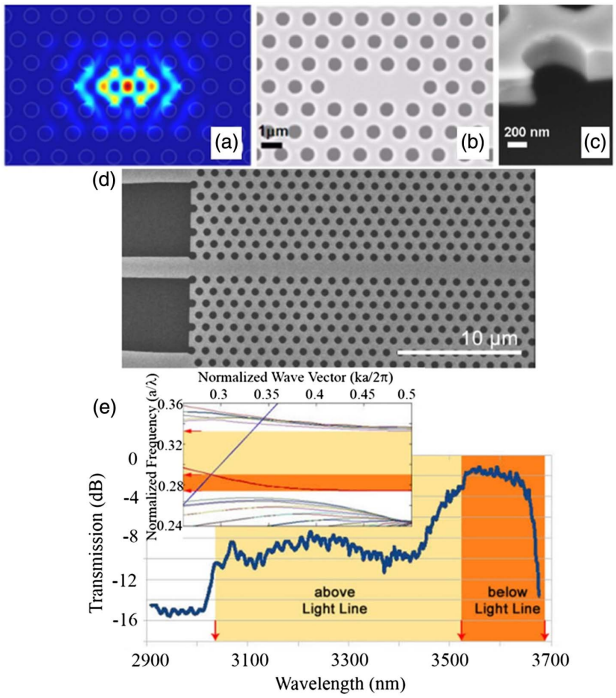

Fig. 7. Suspended-membrane-based PCs on an SOI platform. (a) Mode profile of E_z field component of L3 PC cavity with lattice constant $a = 1.34$ μm, radius $r = 0.263a$, silicon layer thickness $t = 0.5$ μm, and shift of the two edge holes of the cavity $s = 0.15a$, with resonance wavelength of 4.604 μm and Q factor of 24,000 [88]. (b) and (c) SEM images of fabricated device: (b) L3 PC cavity; (c) 45° tilt view of etched side wall of PC cavity hole [88]. (d) SEM image of an MIR W1 PCW [89]. (e) Measured transmission of a PCW with lattice period $a = 1060$ nm. Three colored regions, both in the spectrum and the simulated band diagram (inset), correspond to guided region, above the light line, and bandgap, respectively [89]. Figures are reproduced from: (a)–(c) Ref. [88]; (d) and (e) Ref. [89].

and scanning the wavelength, the highest group index ~12 was measured. The measured propagation loss, using the cut-back method, was about 20 dB/cm at group index about 5 at $\lambda = 3.4$ μm.

2. Suspended-Subwavelength-Grating-Waveguide-Based Devices

Even though several works have been reported using SM-based devices, the two-step process actually complicates the device fabrication. On the other hand, trade-offs involving device performance, the thickness of the residual slab, and etch depth need to be considered. SWG-based devices have been intensively investigated recently for the design flexibility provided in refractive-index engineering, guiding-mode profile engineering, group-index engineering, and so on [90–96]. By tuning the duty cycle (hole/silicon width), SWG can provide a desired effective subwavelength refractive index. Based on this idea, Soler Penadés *et al.* proposed and demonstrated the first suspended SWG waveguide in 2014 [35]. The SWG structure serves three functions: first, it provides lower refractive index for better confinement of the light inside the center core region; second, the SWG fins establish the connection between the

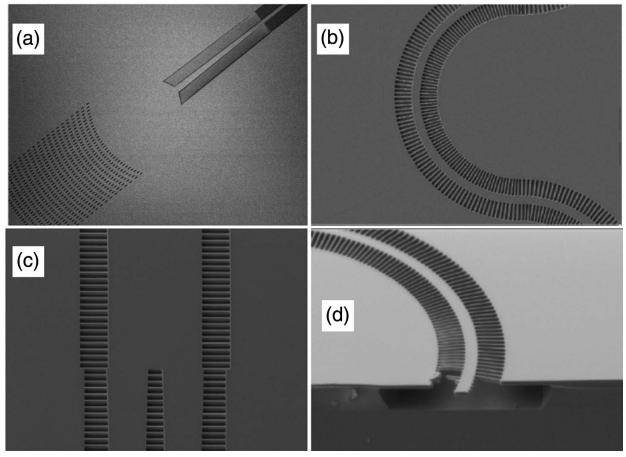

Fig. 8. Suspended-subwavelength-grating-waveguide-based devices on an SOI platform. SEM images of (a) a waveguide with SWG cladding, focusing coupling grating, and taper [35]; (b) the 90° bend [97]; (c) the MMI [97]; (d) a cleaved facet of a 90° bend [97]. Figures are reproduced from: (a) Ref. [35]; (b)–(d) Ref. [97].

core and the surrounding structure, thus providing mechanical stability; third, the holes inside the SWG structure open the channels through which the chemical wet etchant can infiltrate and remove the buried oxide. Also, compared with the SM-based devices, suspended SWG-based devices can be fabricated using one-step etch, and the devices are more robust since the thickness of the silicon layer is constant. Soler Penadés *et al.* demonstrated two types of suspended SWG-based TE waveguides at $\lambda = 3.8$ μm: one with a 300-nm grating period and 150-nm hole size, showing 3.4 dB/cm propagation loss, the other with a 550-nm grating period and 450-nm holes, showing 3.6 dB/cm propagation loss [35]. Focusing coupling grating and taper were demonstrated together [Fig. 8(a)] [35]. The improvement of device performance to 0.82 dB/cm at 3.8 μm was reported by widening the core from 1.1 to 1.3 μm for better confinement and reduction of electron-beam spot size from 20 to 4 nm for side-wall-roughness reduction [97]. Additionally, several basic building blocks based on this structure have been demonstrated, including waveguide bends, MMI devices, and MZIs for $\lambda = 3715$–3800 nm [Fig. 8(b)] [97]. The measured bending loss is below 0.02 dB, specifically 0.014 dB/bend for 90° bends with a radius of 15.7 μm and 0.01 dB/bend for S-bends with 41-μm length and 7-μm offset. Insertion loss and imbalance of the MMI are ~1.6 dB and 0.5 dB, respectively, in the wavelength range of $\lambda = 3720$–3800 nm. Incorporating into an asymmetrical MZI, whose length difference is 350 μm, they measured FSR of ~9.6 nm and ER > 15 dB.

We conclude this section in the following Table 2, listing all reported MIR silicon devices on SOI with free-standing configurations. The measurement results of these devices are also summarized in the table.

3. SILICON-ON-SAPPHIRE

SOS platforms are considered as an alternative platform in MIR since they are commercially available, have a high refractive

Table 2. Devices and Applications on SOI with Free-Standing Structure

Basic Devices	Performance in MIR (Propagation Loss, Q, Coupling Efficiency)	Passive Applications	Active Applications
SM-based waveguides [77,82]	3 dB/cm for TE at $\lambda = 2.75$ μm [77]	N/A	Photodetector with 0.13 A/W responsivity at 1.5 V bias at 2.75 μm [82]
SM-based grating couplers [77]	24.7% coupling efficiency for TE mode at $\lambda = 2.75$ μm [77]	N/A	N/A
SM-based resonators [78,81,83,84]	$Q \sim 8100$ at $\lambda = 2.75$ μm [78]; $Q \sim 2700$ at $\lambda = 5.2$ μm [83]; ~7900 at $\lambda = 3.4$ μm [83]; $Q \sim 83,000$ at $\lambda = 3.79$ μm [84]	Photothermal spectroscopy [81]	N/A
SM-based PCs [87–89]	$Q \sim 13,600$ at $\lambda = 4.4$ μm [88]; $Q \sim 45,000$ at $\lambda = 4.5$ μm [87]; 20 dB/cm at group index ~5 at $\lambda = 3.4$ μm [89]	N/A	N/A
SOI Suspended-SWG-based devices [35,97]	3.4 dB/cm [35] and 0.82 dB/cm [97] at $\lambda = 3.8$ μm; 0.014 dB/90° bend [97]; MMI insertion loss 1.6 dB, imbalance 0.5 dB [97]; asymmetrical MZI FSR 9.6 nm, ER > 15 dB [97]	N/A	N/A

index contrast (~1.7) between the core and the undercladding sapphire, and have a wide transmission window up to $\lambda = 5.5$ μm. In fact, SOS was the first technology used in the electronics industry as an alternative to bulk silicon [98] for the highly insulating sapphire substrate, which provides low parasitic capacitance, low power consumption, higher linearity, and better isolation when compared to bulk silicon [99]. Even though SOS does not compete with SOI in the cost or volume of manufacturing, it is much more mature compared to other platforms, and it does not require special fabrication technologies. All these characteristics facilitate PIC development on SOS platforms. Therefore, the number of demonstrations on SOS platforms is second only to SOI among all MIR silicon platforms.

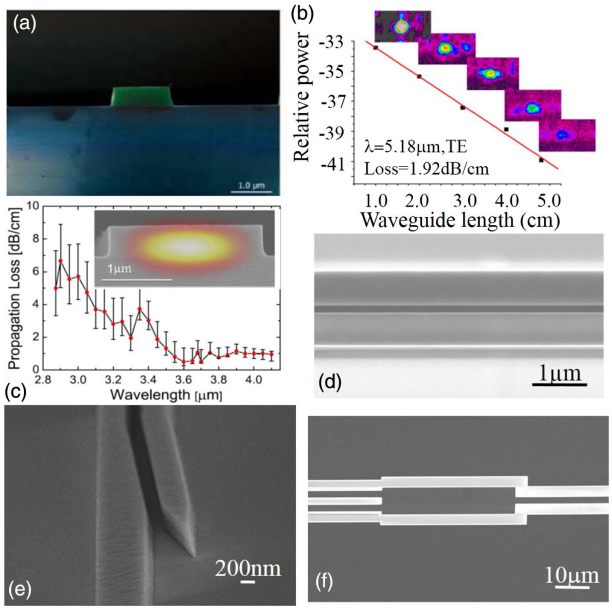

Fig. 9. Waveguides on an SOS platform. (a) False-colored SEM image of the cleaved facet of a waveguide. Here silicon is in green while sapphire is in blue [100]. (b) Cut-back loss measurements at $\lambda = 5.18$ μm for TE polarization along with imaged mode profiles for each length [101]. (c) Ridge waveguide propagation loss for wavelengths ranging from 2.9 to 4.1 μm. Inset shows the cross section of 2400 nm by 480 nm [102]. (d) SEM image of a fabricated slot waveguide working at 3.43 μm wavelength [103]. (e) Close-up of strip waveguide to slot waveguide mode converter [103]. (f) 1 × 2 MMI-based power splitter [104]. Figures are reproduced from: (a) Ref. [100]; (b) Ref. [101]; (c) Ref. [102]; (d) and (e) Ref. [103]; (f) Ref. [104].

A. Devices on SOS Platforms

1. Waveguides

The first MIR SOS waveguide was demonstrated by Baehr-Jones *et al.* in 2010 [100]. Standard fabrication procedure was used to pattern single-mode strip waveguides in SOS [Fig. 9(a)]. TE-polarized light at $\lambda = 4.5$ μm was generated by an optical parametric oscillator (OPO) and guided by a single-mode MIR fiber before it reached the chip. Edge coupling was used to couple light into waveguides. The coupling loss was around 18 dB/facet. Cut-back measurements proved the propagation loss was about 4.3 ± 0.6 dB/cm [100]. The same group also published the propagation loss about 4.0 ± 0.7 dB/cm at $\lambda = 5.5$ μm for TE-polarized light using the same characterization technique [105]. In 2011, Li *et al.* reported a low-loss SOS waveguide at $\lambda = 5.18$ μm [101]. The waveguides are channel-type waveguides whose dimensions are 280 nm in height and 1000 nm in width, covered by SiO_2. TE-polarized light from a quantum cascaded laser passed through a piece of chalcogenide single-mode fiber and was coupled into a testing waveguide. The output was then imaged on an MIR camera using a ZnSe MIR objective lens. Cut-back measurements showed ~1.92 dB/cm propagation loss [Fig. 9(b)] [101]. The low propagation loss is unexpected given the top cladding SiO_2 is highly absorptive at this wavelength and the thin Si core layer (280 nm thick), in which the guiding mode will experience more twinning defects inherent in SOS [99]. Our group published propagation loss results for an SOS strip waveguide at 3.43 μm in 2014 [103]. The TE-polarized light from commercially available interband cascaded laser (ICL) was first coupled into a single-mode ZrF_4 optical fiber by a pair of ZnSe lenses. The guided light was then coupled into the waveguide through an SWG coupler. The output signal from the output SWG was coupled into the output

fiber and measured by a liquid-nitrogen-cooled InSb detector. During the whole measurement, in order to improve the signal-to-noise ratio, a mechanical chopper was used with chopping frequency of 1 kHz, and the detected signals from InSb were demodulated by a lock-in amplifier. About 2.1 dB/cm propagation loss from the cut-back measurement was observed [103]. Methods for improving waveguide performance in SOS were reported by Shankar *et al.* [106]. A resist-reflowing process consisted of a 5-min post-lithography bake in an oven at 140°C and a piranha etch-hydrofluoric (HF) acid cycling-based post-fabrication process were employed to reduce side-wall-roughness-induced scattering loss. Therefore, the Q from a ring resonator was greatly improved. The propagation loss about 0.74 dB/cm at $\lambda = 4.5$ μm can be deduced from the measured Q [106]. Other than these works, SOS waveguides have also been demonstrated at $\lambda = 2.75$ μm together with grating couplers at that wavelength [107]. In 2015, Singh *et al.* reported propagation losses of a ridge waveguide at wavelengths ranging from $\lambda = 2.9$ to 4.1 μm [102]. The ridge waveguide was a multi-mode waveguide with 2400-nm width and 480-nm height [Fig. 9(c)]. End-fire coupling was used, showing 9 dB/facet loss.

The geometry of slot waveguides can push the guided mode into the central low-index region, so more light–matter interaction can be expected compared with strip waveguides. Therefore, slot waveguides have a lot of important applications and are a very important and basic building block for integrated photonics. We demonstrated the first SOS slot waveguide [Fig. 9(d)] in 2014 [103]. The confinement factor that characterizes the portion of energy within the low-index region is a very important value for slot waveguide design. We scanned the slot width and two silicon rail widths to achieve the optimized confinement factor using FIMMWAVE software from PhotonDesign. High confinement (about 43%) was obtained in the slot when the rail width is 600 nm and slot width is 130 nm. Propagation loss of 11 dB/cm was experimentally obtained for slot waveguides using the cut-back method. Since the electric field distribution is quite different from the field distribution inside the strip waveguide, an efficient strip-to-slot waveguide mode converter is desired. A robust and efficient two-step taper was used to smoothen the transition from strip-waveguide mode to slot-waveguide mode [Fig. 9(e)]. The conversion efficiency of our strip-to-slot waveguide mode converters is realized by measuring the loss from several cascaded mode converters, showing a loss of about 0.13 dB per mode converter, corresponding to 97% conversion efficiency. The details regarding device design and experimental methods for fabrication and measurement can be found in Ref. [103].

Power splitters are also very critical in integrated photonics. A 1 × 2 MMI power splitter in SOS was demonstrated in 2015 [104]. The MMI was designed to be 11 μm wide and 51 μm long to split the light into two arms equally [Fig. 9(f)].

2. Grating Couplers

Due to the absence of an efficient silicon light source, most on-chip silicon devices need input from an external light source via an optical fiber or free space. Recently, MIR single-mode fiber has become commercially available [108] and is expected to facilitate MIR PIC research. However, there is a big mismatch between the optical modes inside silicon-based waveguides and fiber both in size and distribution. To solve this issue, a grating coupler is highly desired. The first grating coupler on an SOS platform was reported by Cheng *et al.* in 2012 [107]. They proposed several grating couplers for coupling between the TE/TM mode in an SOS waveguide and fluoride-based fibers, and, in experiments, they demonstrated a coupling efficiency of 32.6% for a TE-mode shallow-etch uniform grating coupler [Figs. 10(a) and 10(b)] and 11.6% coupling efficiency for a TM-mode SWG coupler [Figs. 10(c) and 10(d)] at the wavelength of 2.75 μm [107].

While shallow-etch requires two exposures and etch steps, which complicates the fabrication process, in order to efficiently couple light into/out from the chip, we designed SWG couplers working for the TE mode at $\lambda = 3.43$ μm, following the design rules we developed in the NIR [93,109] with coupling areas that match with the fiber mode cross section [103]. It is worth noting that while SWG couplers for the TM-polarized mode have been experimentally demonstrated by other research groups, our work primarily focused on TE polarization due to design requirements in horizontal slot waveguides and hole-type PCW structures that function only with TE polarization with an in-plane electric field. At $\lambda = 3.43$ μm, the SWG has a period of 1500 nm in the propagation direction and duty cycle of 45%. Inside the subwavelength region, our optimized design had a rectangular air trench width, length, and period as 152, 825, and 800 nm, respectively, which resulted in an effective subwavelength index ~2.45 [Figs. 10(e) and 10(f)]. The optimized geometry provided 36% coupling efficiency for TE-polarized light from fiber to SWG coupler near $\lambda = 3.43$ μm, and the peak emission angle is about 11° from normal incidence. For coupling efficiency measurement on the SWG, we connected the two couplers with a multimode waveguide. Assuming propagation loss in the multimode waveguide is negligible, and assuming the two SWG couplers are identical, we extracted the coupling loss of one grating coupler as half of the insertion loss. The peak coupling efficiency, about 29%, is at an 11° angle from the normal.

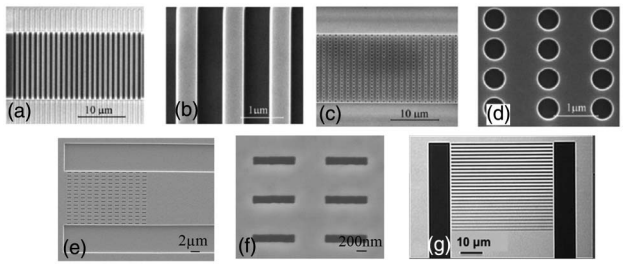

Fig. 10. Grating couplers on an SOS platform. (a) SEM image of shallow-etched uniform grating on the 10-μm-wide waveguide [107]. (b) Zoom-in image of (a) with 405-nm etch depth, 0.4 fill factor, and 1120-nm period [107]. (c) SEM image of full-etched nanoholes subwavelength grating on the 10-μm-wide waveguide [107]. (d) Zoom-in image of (c) with 600 nm etch depth, 253 nm nanoholes radius, and 1250 nm period [107]. (e) SEM image of full-etched subwavelength grating coupler [103]. (f) Magnified view of air holes in (e) with 152 nm width, 825 nm length while the periods in vertical and horizontal directions are 800 nm and 1500 nm, respectively [103]. (g) Optical image of a fully etched 1D grating coupler [106]. Figures are reproduced from: (a)–(d) Ref. [107]; (e) and (f) Ref. [103]; (g) Ref. [106].

A full-etched uniform grating coupler with theoretical coupling efficiency of 40% and bandwidth of 150 nm for coupling between an SOS waveguide and the free-space laser beam was also reported by Shankar *et al.* [106]. The operating wavelengths are between $\lambda = 4.3$ and 4.6 μm using multiple grating couplers with different geometries [Fig. 10(g)].

3. Ring Resonators

Ring resonators have also been demonstrated on the MIR SOS platform [105,106,110]. The first MIR SOS ring resonator was reported in 2010 by Spott *et al.* [105]. The ring had a 40-μm radius and 0.25-μm edge-to-edge space [Fig. 11(a)]. The measurement results showed $Q \sim 3000$, FSR around 29.7 nm, and associated group index ~3.99, for wavelengths of $\lambda = 5.4 - 5.6$ μm [105].

In 2013, a report regarding waveguide performance improvement was published [106]. The waveguide propagation loss was significantly reduced through the resist-reflow and post-fabrication processes, piranha etch/HF cycling, and annealing. This led to a high intrinsic Q (~278, 000) of the ring resonator (60 μm in radius) at $\lambda = 4.35$–4.6 μm wavelength range [Fig. 11(b)].

Using a single wavelength probe laser ($\lambda \sim 2.75$ μm) and combined thermal tuning to characterize a ring resonator in SOS was reported by Wong *et al.* [110]. They scanned the temperature-dependence transmission [Fig. 11(c)] first and calculated the Q of the ring to be about $11,400 \pm 800$ at $\lambda \sim 2.75$ μm using the TO coefficient in the literature.

4. Photonic Crystal

Slow light in PCWs has been well understood and can be utilized to reduce the optical absorption path length and achieve high detection sensitivity in on-chip optical absorption spectroscopy [111]. A conventional W1 PCW [Fig. 12(a)] for TE-polarized light with a single missing row of holes along the $\Gamma - K$ direction in a hexagonal lattice of air holes in SOS was reported [112]. The top cladding is air, and the bottom cladding is sapphire. An adiabatic group-index taper [110,113,114] was also used by gradually tapering down the width of the PCW from the interface between the strip waveguide and PCW over eight lattice periods from W1.07 to W1. W1.07 indicates that the width of the PCW at the onset of the taper is $1.07 \times \sqrt{3}a$. Here a indicates lattice constant. The coupling loss due to huge group-index mismatch can be significantly reduced via adiabatic tapering. To overcome the availability of a broadband source or a tunable laser in MIR, a unique method to characterize the W1 PCW by lattice constant tuning using a single wavelength source at $\lambda = 3.43$ μm wavelength, to specifically identify designs for waveguiding in the high group-index transmission pass bands of the PCW, was developed [112]. Combined with the propagation-loss measurement, the true photonic-band-gap (PBG)-guided W1 transmission was identified for lattice constants between 845 nm and 850 nm, with losses around 12 dB/cm.

Conventional PCW can slow down the propagating light and enhance the light–matter interaction in the temporal domain. However, if we take a look at the mode profile of PCW, only a small portion of the guiding mode has real interaction with outside analytes. In order to increase the spatial overlap integral between light and the analyte, special designs are needed. By introducing PC lattice defects, like rectangular slots [Fig. 12(b)] or circular slots (holes) [Fig. 12(c)], in the PCW, the slotted PCWs [Fig. 12(b)] or holey PCWs (HPCWs) [Fig. 12(c)] were demonstrated [115]. Measurements showed that HPCWs were significantly less lossy than slotted PCWs that are extensively studied in the NIR. Since adding defect holes into PCW will move the guiding mode towards a higher frequency, to compensate for the transmission bandwidth decrease, a wider PCW from W1 to W1.2 was used. Details of the parameter selection are given in Ref. [115]. A similar strategy of

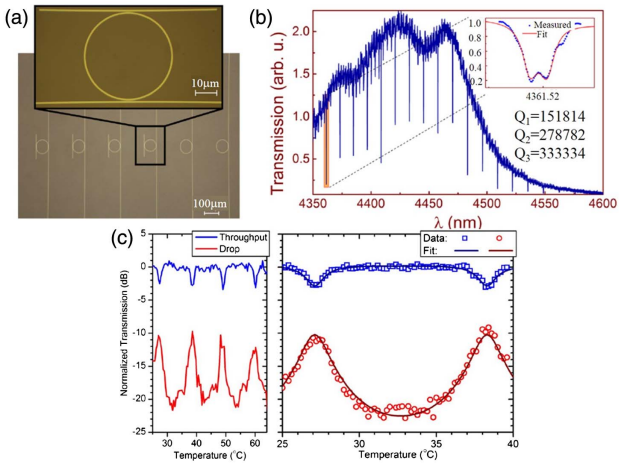

Fig. 11. Ring resonators on an SOS platform. (a) Optical micrographs of the primary MIR ring resonator with $Q \sim 3,000$ around $\lambda = 5.45$ μm wavelength (top) and a group of ring resonators with various dimensions (bottom) [105]. (b) Transmission ($\lambda = 4.35$–4.6 μm) of a ring resonator after resist-reflow and post-fabrication treatment, showing loaded $Q_l \sim 151,000$, and intrinsic $Q_0 \sim 278,000$ (inset) [106]. (c) Normalized temperature-dependent transmission of a quasi-TE ring resonator working at $\lambda = 2.75$ μm at 25°C–65°C scanning (left) and 25°C–40°C scanning (right) [110]. Figures are reproduced from: (a) Ref. [105]; (b) Ref. [106]; (c) Ref. [110].

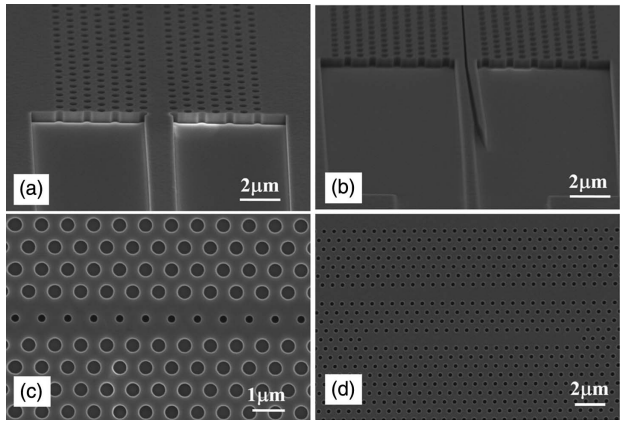

Fig. 12. PCs on an SOS platform. (a) Side view SEM image of the W1 PCW at the PCW-strip waveguide interface [112]. (b) 70° tilt view of the slot mode converter at the input (or output) of the slotted PCW [115]. (c) Top view SEM image of the HPCW [115]. (d) Top view of an L21 PC microcavity side coupled to W1.05 PCW [104]. Figures are reproduced from: (a) Ref. [112]; (b) and (c) Ref. [115]; (d) Ref. [104].

adiabatic group-index taper design as the W1 PCW was used to reduce the insertion loss in the HPCW. Compared with W1 PCW, the guiding mode is concentrated in the holes rather than the silicon, so more field can interact with the testing analytes. It is also noted from the field cross section that the peak field enhancement in the circular slots at the center of the HPCW is almost 3.5 times stronger than the peak field in a W1 PCW. A similar characterization method was used, and the true PBG guided mode was experimentally observed for lattice constants between 830 nm and 850 nm, with propagation loss around 14 dB/cm.

A PCW coupled PC microcavity was reported at $\lambda = 3.43$ μm on an SOS platform by our group in 2015 [104]. The PC microcavity investigated is linear L*n*-type, and *n* denotes the number of missing air holes in a row parallel to the W1.05 PCW. A similar structure has been used extensively for biosensing in SOI in the NIR [116,117]. Again, light-line position, stop gap, and guided-mode transmission behavior were characterized using a fixed-wavelength laser source through the lattice constant tuning method. The lattice constant for an L21 PC microcavity coupled to the W1.05 PCW was set as 820 nm according to the transmission measurement. The resonance of an L21 PC microcavity was characterized by thermal tuning of the cavity resonance across the source wavelength, showing a quality factor of ~3500 [104].

5. SOS Wafer Challenges

It is instructive to note here that SOS wafers suffer from a fundamental limitation of high dislocation defect densities at the silicon–sapphire interface. Figure 13 shows a typical transmission electron microscope (TEM) image of a commercially available SOS wafer that shows faults along the $\bar{1}100$ orientation. The defects are most pronounced up to the first ~200 nm from the silicon–sapphire interface. Annealing does not significantly improve the situation, as shown in Fig. 13(b). Extremely high propagation losses exceeding 10 dB/cm were thus experimentally observed in 350-nm-tall and 2500-nm-wide waveguides in both the NIR and MIR. The low propagation losses observed experimentally in SOS waveguides, at least 600 nm thick, indicate that the thicker SOS is still promising for MIR PIC applications.

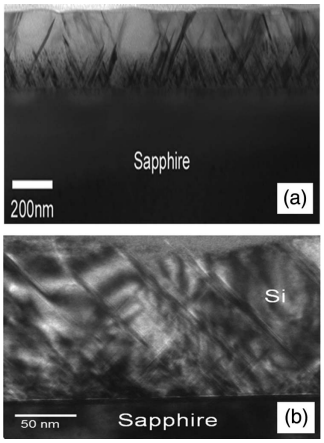

Fig. 13. TEM images of SOS wafer (a) before and (b) after annealing.

B. Device Applications

1. Sensing

So far, not only the above-mentioned basic devices on SOS platforms have been demonstrated, but also the applications of these devices. Our group, in 2015, demonstrated an on-chip absorption sensor for gas-phase TEP (triethylphosphate, $C_6H_{15}O_4P$) that has a strong absorption peak at $\lambda = 3.43$ μm [115]. At room temperature, TEP is a chemical in liquid phase. In order to sense it in the gas phase, a commercial Kin-Tek vapor generator was used to provide a measured quantity of TEP by controlling the gas flow of nitrogen and the TEP vapor. When the TEP is heated up to 70°C, the vapor is released via heated tubing at a height of approximately 1–2 mm from the surface of the testing chip to mimic a field version of the system with gas being sensed in free space. The chip surface was also heated to 70°C to ensure that the vapors of TEP did not condense onto the surface of the chip. An 800-μm-long HPCW with $a = 845$ nm was chosen, which, as mentioned in the previous subsection, combined both large mode overlap and slow light effect (calculated group index $n_g = 20$ at $\lambda = 3.43$ μm), and the transmitted light intensity through the device in the presence and absence of TEP was recorded and plotted, as shown in Figs. 14(a) and 14(b). For measurement accuracy, before the TEP was on, the hot nitrogen gas flowed through the heated tubing from a gas generator to the top of the chip surface at the same flow rate, so that when the TEP flow was turned on, the only change to the transmitted power was from adding TEP molecules to the nitrogen flow stream. As seen from Fig. 14(a), the transmitted signal intensity drops to 80% of its original intensity, indicating the presence of TEP, and in Fig. 14(b), the steady state intensity in the presence of TEP is about 60% of its original intensity when the concentrations of TEP were 10 parts per million (ppm) and 50 ppm, respectively. As a comparison, when HPCW was replaced by a slot waveguide with the same length, as shown in Figs. 14(c) and 14(d), no intensity drop could be observed when the TEP concentration was 25 ppm, but around a 20% drop could be found when the concentration was increased to 28 parts per hundred (pph). Furthermore, when replacing with a strip waveguide, no change was observed [Fig. 14(e)] even when the concentration was 28 pph. It is also worth noting that significant signal margin exists in Fig. 14(a) to allow detection of TEP concentrations lower than 10 ppm.

A gas sensor using an SOS ring resonator was also reported [118]. Nitrous oxide (N_2O) gas with 5000 parts per million by volume (ppmv) concentration was detected using a 120-μm radius ring resonator at wavenumber of 2241.79 cm^{-1} (corresponding to $\lambda = 4.46$ μm) [Fig. 14(f)]. When N_2O is introduced, if the resonator line overlaps N_2O absorption due to the addition loss, the resonance Q will decrease [Fig. 14(g)]. If the resonator line does not overlap with the N_2O absorption peak, the Q remains the same. Therefore, concentration of N_2O can be calculated from the measured Q difference before and after N_2O flow.

Recently, Singh *et al.* demonstrated an SOS-based device for heavy water (D_2O) sensing at around $\lambda = 4$ μm [119]. A 3-μm-wide multi-mode waveguide was employed to reduce the propagation loss to the fundamental mode by reducing its interaction to the side-wall roughness. In order to avoid

complete absorption of the propagating light by the H_2O and D_2O mixture, with absorption coefficients of 144 cm^{-1} and 18,000 cm^{-1}, respectively, around $\lambda = 4$ μm [120], 1.2-μm-thick SiO_2 was deposited on top of the SOS. Measured transmission showed that concentrations up to 0.25% of D_2O in the H_2O and D_2O mixture can be detected [Fig. 14(h)].

2. Optical Switch

Other than MIR sensors, an SOS-based optical switch has also been reported [121]. The switch was a PCW incorporated MZI structure, which utilizes the slow light property of PCW to improve light–matter interaction and shrink down the device size. Each arm of the MZI had an 80-μm-long PCW on it [Fig. 15(a)]. The switch mechanism is based on the silicon TO effect. The PCW is a W1.05 PCW with radius of the PC air holes $r = 0.225a$. The modified design versus Ref. [112] gives a 40-nm PCW guided-mode bandwidth compared to a 22-nm guided-mode bandwidth previously. Only one gold heater was used and placed adjacent to one PCW as in Fig. 15(a). The heater was fabricated by adding an additional metal liftoff process after the silicon device fabrication. An MMI with the same design as in the previous publication [104], shown in Fig. 9(f), 11 μm wide and 51 μm long, was implemented at both the input and the output, to respectively split the light equally into and combine the light equally from the two arms of the symmetric MZI. When applying DC power to the heater, the generated heat diffuses into the adjacent PCW region and causes a change in the refractive index. The index change induces a change in the phase of the transmitted light through the adjacent PCW. Since the phase change of the transmitted light is a ratio to the slowdown factor for fixed refractive index change, the slow light effect from PCW actually enhances modulation efficiency and thus shrinks the device length [122]. Figure 15(b) plots the normalized optical intensity against the applied power at $\lambda = 3.43$ μm. A maximum modulation depth of 74% was obtained for a switching power of 170 mW. A completely symmetric structure, which has micro-heaters on both the reference and signal arms of the MZI, may help increase the modulation depth through equalizing the optical intensity of the two interfering beams.

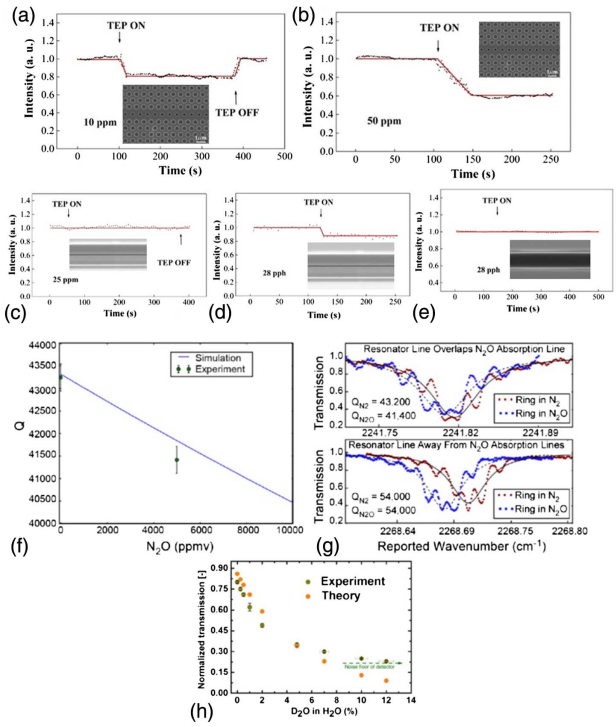

Fig. 14. Sensing application of devices on an SOS platform. Change in transmitted light intensity at $\lambda = 3.43$ μm through silicon devices in SOS for TEP sensing: an 800-μm-long HPCW with lattice constant $a = 845$ nm with introduction of (a) 10 ppm TEP and (b) 50 ppm TEP; an 800-μm-long silicon slot waveguide when introducing of (c) 25 ppm TEP and (d) 28 pph TEP; (e) a silicon strip waveguide in the presence and absence of 28 pph TEP [115]. (f) Comparison of theoretical and measured Q of a MIR ring resonator in zero and 5000 ppmv N_2O [118]. (g) Zoom-in spectral of resonance variation in pure N_2 and in 5000 ppmv N_2O concentration. The upper/lower panel corresponding to resonator line overlaps/away from N_2O absorption line [118]. (h) Normalized transmission of a 3-μm-wide multi-mode strip waveguide with 1.2-μm-thick SiO_2 up cladding at different D_2O–H_2O mixtures [119]. Figures are reproduced from: (a)–(e) Ref. [115]; (f) and (g) Ref. [118]; (h) Ref. [119].

3. Nonlinear Applications

As mentioned in Section 2, nonlinear effects in a silicon waveguide have a number of applications, such as SCG and wavelength conversion. Unlike in an SOI platform, where several nonlinear applications have been reported, on SOS platforms, so far, only SCG using a silicon rib waveguide has been demonstrated by Singh *et al.* [102]. The waveguide they used is shown in Fig. 9(c) with a cross section of 2400 nm by 480 nm, which can provide an optimal dispersion (low and anomalous) for the TE mode at the pump wavelength in the region where multi-photon absorption and linear propagation losses are low. A 320-fs pulse at $\lambda = 3.7$ μm at a repetition rate of 20 MHz was coupled into the waveguide through end-fire coupling. The output spectra were collected through a monochromator and detected with two MIR detectors with different operating ranges (PbSe at 1.5–4.8 μm and MCT at 4–6.5 μm). The spectra shows a broad generated spectrum when pump peak power ranges from 200 W to 2.5 kW [Fig. 16(a)]. The widest continuous spectrum at the −30 dB signal level is 1.53 octaves, from $\lambda = 1.9$–5.5 μm, when the pump power was 1.82 kW. If considering a −45 dB signal level, the generated light is beyond $\lambda = 6$ μm. Nonlinear transmission as a function of coupled intensity was also measured [Figs. 16(b)–16(e)]. The onset of nonlinear loss occurred near 1 GW/cm^2, and the transmission was strongly saturated near 10 GW/cm^2. The major cause of the nonlinear loss came from four-photon absorption.

It is instructive to mention here that several simulation works, such as MIR SCG using pillar waveguides [123], wavelength conversion for indirection detection of MIR signals [124], MIR Raman amplification and wavelength conversion [125], and MIR cross-phase modulation [126], have been reported on an SOS platform.

Table 3 summarizes all the demonstrated devices on SOS platforms, including basic waveguides, slot waveguides, grating couplers, ring resonators, PCW, PC cavities, as well as some demonstrated applications using the above basic devices. These fundamental research works provide realization of the basic components for future MIR PICs on SOS.

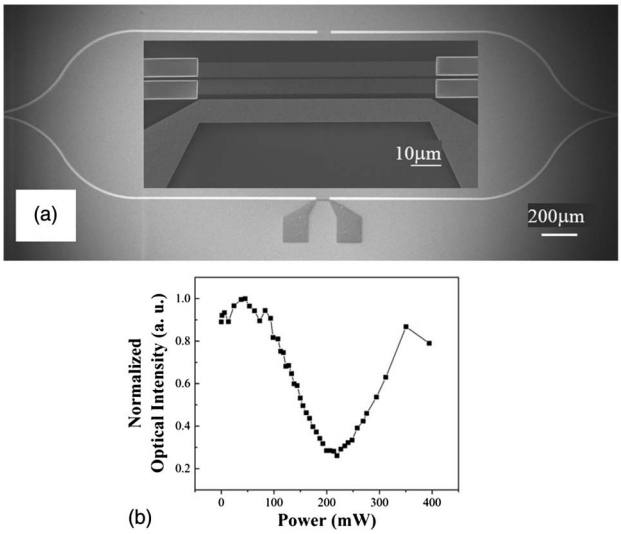

Fig. 15. MIR PC TO switch. (a) SEM image of the whole MZI structure; the gold heater is adjacent to one PCW on one arm. Inset shows the zoom-in image of the heater and PCW [121]. (b) Normalized optical intensity from the TO switch against applied heating power at $\lambda = 3.43$ μm [121]. Figures are reproduced from Ref. [121].

4. STANDARD SILICON WAFER

The other platform for MIR silicon photonics is the standard silicon wafer, which is the most common and cheapest wafer in the microelectronics industry. However, due to lack of vertical refractive index contrast, without special treatment it cannot provide waveguiding. One approach to creating such index contrast is through doping. However, two drawbacks limit this method in MIR. The first is that the created contrast is too small for device miniaturization, and the second is the loss from doping-induced free-carrier limits device performance. Therefore, researchers have proposed several new ways to solve these two issues and have demonstrated waveguides on standard silicon wafers in MIR. Their results showed that by special design and fabrication processes, optical modes can be confined in certain region with low surrounding materials, enabling MIR optical guiding mechanism.

A. Suspended-Membrane-Based Waveguides

The first type of MIR silicon waveguide on a standard silicon wafer was the suspended rib waveguide. The working principle is the same as that of the SM waveguide on SOI mentioned in Section 2, which confines the light only at the center rib region with air as the top and bottom claddings [78]. SM waveguides on standard silicon wafers were demonstrated in the NIR using the undercut method [127]. The first MIR suspended-membrane waveguide in a standard silicon wafer was demonstrated by Chiles *et al.* in 2013 [34]. The suspended membrane was formed through a wafer bonding process, and the rib waveguides were patterned in the suspended membrane using standard lithography and reactive ion etching (RIE) [Fig. 17(a)]. The fabricated waveguides [Fig. 17(b)] were 2.4 μm wide and had ribs that extended by 1.07 μm above the membrane. The membrane width was 17 μm wide, and the residual slab was 1 μm thick. The waveguides were characterized using the Fabry–Perot (FP) resonance technique [128], and propagation losses of 4.0 ± 1 dB/cm and 2.8 ± 0.5 dB/cm for TE and TM, respectively, at $\lambda = 3.39$ μm wavelength were observed.

B. T-Guides

The second type of MIR silicon waveguides on standard silicon wafer are so-called T-guides, which were also demonstrated by the same group in 2016 [129]. A similar wafer bonding process was adopted to transfer the silicon membrane from an SOI to a patterned silicon wafer and form the slab shown in Fig. 17(c). Here the T-guide has a 1.3-μm slab thickness and 1.8-μm post width. Using the cut-back method, they obtained a TE-mode propagation loss of 1.75 ± 0.3 dB/cm and 2.7 ± 0.5 dB/cm for 1.79 μm and 1.52 μm post widths at $\lambda = 3.64$ μm wavelength [Fig. 17(d)]. Simulation results also showed the potential of supporting a single mode and single polarization from $\lambda = 1.2$–8.1 μm, which is nearly the entire span transmission window of silicon [129]. Compared with SM-based

Table 3. Summary for Devices on SOS

Devices and Related Works	Device Performance: Propagation Loss; Coupling Efficiency; Quality Factor (Q)	Applications and Performance
Strip/channel/ridge waveguides [100–103,105–107,119]	4.3 dB/cm (TE at $\lambda = 4.5$ μm) [100]; 4 dB/cm (TE at $\lambda = 5.5$ μm) [105]; 1.92 dB/cm (TE at $\lambda = 5.18$ μm) [101]; 2.1 dB/cm (TE at $\lambda = 3.43$ μm) [103]; 0.74 dB/cm (at $\lambda = 4.5$ μm) [106]	0.25% D_2O sensing [119]; 2–6 μm supercontinuum generation [102]
Slot waveguide [103]	11 dB/cm at $\lambda = 3.43$ μm [103]	28 pph in TEP sensing [103]
Grating coupler [103,106,107]	SWG: 29% for TE mode at $\lambda = 3.43$ μm [103]; 11.6% for TM at $\lambda = 2.75$ μm [107]; shallow-etched uniform grating coupler: 32.6% for TE at $\lambda = 2.75$ μm [107]	N/A
Ring resonator [105,106,110,118]	$Q \sim 3000$ at $\lambda = 5.5$ μm [105]; 278000 at $\lambda = 4.5$ μm [106]; 11400 at $\lambda = 2.75$ μm [110]	N_2O gas with 5000 ppmv [118]
PCW [112,115,121]	PCW: 12 dB/cm at $\lambda = 3.43$ μm [112]; SPCW: 55 dB/cm at $\lambda = 3.43$ μm [115]; HPCW: 15 dB/cm at $\lambda = 3.43$ μm [115]	HPCW: 10 ppm TEP sensing [115]; PCW based TO switch: 170 mW switching power with 74% modulation depth [121]
PC cavity [104]	$Q \sim 3500$ [104]	N/A

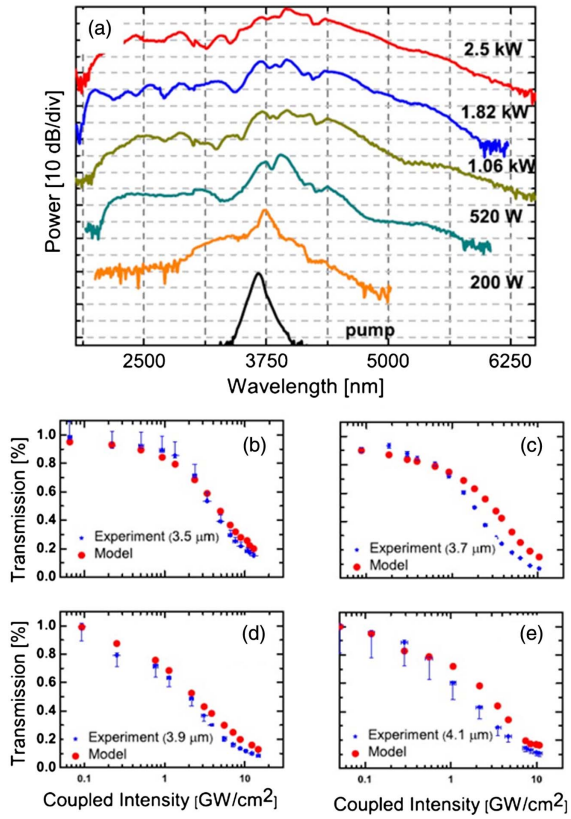

Fig. 16. MIR supercontinuum generation in an SOS waveguide. (a) Experimentally observed output spectra for different coupled input peak powers [102]. (b)–(e) Measured and calculated transmission as a function of coupled intensity at the input of a 5 μm by 0.5 μm SOS waveguide at (b) $\lambda = 3.5$ μm, (c) $\lambda = 3.7$ μm, (d) $\lambda = 3.9$ μm, and (e) $\lambda = 4.1$ μm [102]. Figures are reproduced from Ref. [102].

waveguides, T-guides have better mechanical stability from the post beneath and more design freedom for dispersion engineering.

C. Pedestal Waveguides

Pedestal waveguides are the third type of MIR silicon waveguides on standard silicon wafers, which do not require any SM structure as well as bonding process. This type of waveguide was first demonstrated in the NIR in 2013 by Chang *et al.*, showing comparable propagation loss to conventional SOI-channel waveguides [130]. Lin *et al.* demonstrated the first MIR pedestal waveguide in 2013 [131]. The waveguide was fabricated through three key steps [Fig. 18(a)], including shallow etch for guiding region definition, conformal oxide deposition for guiding region protection, and undercut for preventing guiding mode leakage. The fabricated pedestal waveguides [Fig. 18(b)] were measured in the wavelength region of $\lambda = 2.5$–3.7 μm and showed single-mode guiding characteristic and 2.7 dB/cm propagation loss at $\lambda = 3.7$ μm wavelength. Equal output intensity at 3.2 μm was observed from a pedestal waveguide Y-splitter.

Based on the above-mentioned pedestal waveguides, Lin *et al.* also demonstrated an MIR absorption sensor for several chemicals' detection at $\lambda = 3.3$ μm and $\lambda = 3.55$ μm wavelengths [132]. Since toluene has a strong absorption at $\lambda = 3.3$ μm from the aromatic C–H stretch, when the guiding wavelength at

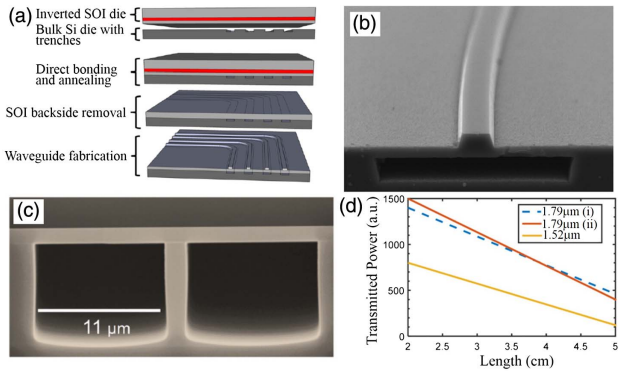

Fig. 17. Standard silicon wafer. (a) Fabrication scheme for producing suspended silicon rib waveguide in a standard silicon wafer [34]. (b) SEM image of a fabricated suspended silicon waveguide with dimensions of 2.4 μm wide and 1.07 μm above the membrane, which is 1 μm thick and 17 μm wide [34]. (c) SEM cross section of an MIR silicon T-guide, which only supports a single mode and a single polarization in the range from 1.2 to 8.1 μm [129]. (d) Measured transmission at different lengths for two different waveguide structures [129]. Figures are reproduced from: (a) and (b) Ref. [34]; (c) and (d) Ref. [129].

$\lambda = 3.3$ μm met toluene, it was absorbed and resulted in output power drop [Fig. 18(c)]. After toluene evaporated, the output power went back to its original level [Fig. 18(c)]. The output intensity shows an inverse ratio to the toluene concentration of the toluene and carbon tetrachloride mixture, where carbon tetrachloride is not absorptive in this region [Fig. 18(d)]. Besides, several other chemicals' absorbance was also measured using the MIR pedestal sensor at $\lambda = 3.55$ μm, showing good agreement with the literature [Fig. 18(e)].

D. Silicon-on-Porous-Silicon

A silicon-on-porous-silicon (SiPSi) platform was proposed for MIR devices in which the waveguide cladding is a porous silicon layer created in the same silicon wafer by high-energy proton-beam irradiation and electrochemical etching [60]. A silicon waveguide 2 μm in height and 4 μm in width [Fig. 19(a)] was characterized by the cut-back method. The results show propagation losses of 3.9 ± 0.2 dB/cm at $\lambda = 3.39$ μm and 2.1 ± 0.2 dB/cm at 1.55 μm, which are slightly higher than those of the conventional waveguides [Fig. 19(b)]. The major loss may come from the material damage and scattering loss caused by the high-energy irradiation. SiPSi has the best mechanical stability among all waveguide types on a standard silicon wafer, but requires accurate control to avoid damage of the guiding region during high-energy irradiation.

Table 4 summarizes the devices demonstrated, so far, on a standard silicon wafer for MIR applications. Several different types of waveguides, which require special design and fabrication process, have been demonstrated, showing compatible propagation loss with other platforms. Applications based on pedestal waveguides in chemical sensing have also been reported.

5. OTHER PLATFORMS

A. Silicon-on-Nitride

As suggested in Refs. [33,133], silicon nitride has a transparent window up to $\lambda = 6.7$ μm. In the meantime, silicon nitride is

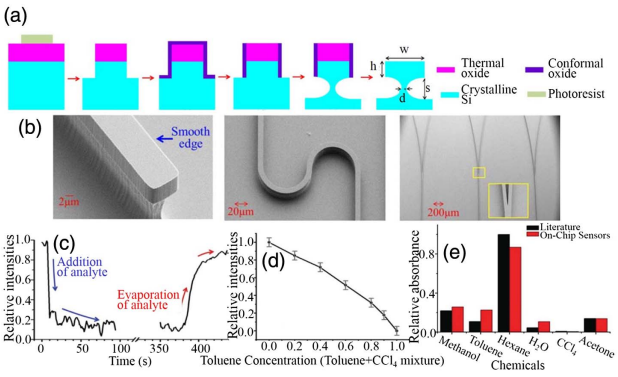

Fig. 18. Pedestal-type waveguides on a standard silicon wafer. (a) Fabrication procedure to make a pedestal-type waveguide [131]. (b) SEM images of fabricated pedestal MIR devices including waveguide, waveguide bending, and Y-splitter [131]. (c) Real-time trace of toluene using a pedestal-waveguide-based MIR sensor, showing output intensity drops when adding analytes and recovers during evaporation of analytes [132]. (d) Output intensity decreases as toluene ratios increase since the aromatic C-H stretch in toluene strongly absorbs the transmitting light at 3.3 μm wavelength [132]. (e) Absorbance of six different chemicals at 3.55 μm [132]. Figures are reproduced from: (a) and (b) Ref. [131]; (c) and (d) Ref. [132].

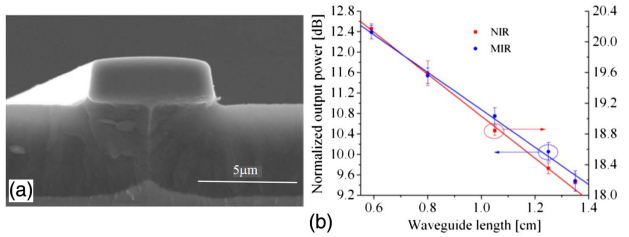

Fig. 19. Silicon-on-porous-silicon. (a) Cross section of a silicon waveguide on porous-silicon bottom cladding [136]. (b) Measured propagation loss for oxidized SiPSi waveguides in both NIR and MIR through the cut-back method [60]. Figures are reproduced from: (a) Ref. [136]; (b) Ref. [60].

also a CMOS-compatible material with refractive index ~2. Using silicon-nitride-on-insulator as an MIR platform has been demonstrated, showing waveguide propagation loss about 2.52 ± 0.1 dB/cm at 2 μm [15], 2.1 dB/cm at 3.7 μm [13], and Q of microring resonators about 3200 at 2 μm [15], about 1×10^6 at 2.6 μm [14], as well as frequency comb spanning from 2.3 to 3.5 μm [14]. The literature also shows, up to $\lambda = 8.5$ μm, silicon nitride has negligible loss [13]. Therefore, silicon-on-nitride (SON) becomes a promising alternative for conventional SOI by replacing the lossy bottom cladding silicon dioxide with silicon nitride. In 2012, Yue *et al.* theoretically investigated the SON waveguide, and showed a low chromatic dispersion [± 50 ps/(nm · km)] in the MIR region of $\lambda =$ 2430–6630 nm [134]. Right after that, Khan *et al.* demonstrated the first MIR waveguide on an SON platform [135]. They bonded a silicon handling die to a low-stress silicon-nitride-coated SOI die and subsequently removed the SOI substrate to build the SON platform, as shown in Fig. 20(a). Silicon single-mode rib waveguides with 2-μm rib thickness, 1.2-μm residual slab thickness, and 2.0–2.5-μm rib widths were fabricated on this platform and tested at $\lambda = 3.39$ μm wavelength, as shown in Fig. 20(b). Using the FP resonance method [128], the waveguides have a propagation loss of 5.2 ± 0.6 dB/cm and 5.1 ± 0.6 dB/cm for TE and TM, respectively [135].

Recently, Spott *et al.* slightly modified the fabrication procedure to create a silicon-on-nitride-on-insulator (SONOI) die, and integrated quantum cascade lasers with SONOI waveguides [Figs. 20(c) and 20(d)] [137]. These lasers are FP lasers, which emitted 4.8-μm light in pulse mode at room temperature. The single-sided output powers as high as 31 mW and threshold currents as low as 387 mA were observed at 20°C [137]. By introducing shallow surface gratings on silicon waveguides [Fig. 20(e)], distributed feedback QCLs heterogeneously integrated with SONOI waveguides were demonstrated by the same group [138]. Selected lasing modes ranging from $\lambda = 4.62$ to 4.86 μm were observed through different grating periods, and the maximum measured output power was 211 mW.

Besides the aforementioned works, an SON slot waveguide was proposed by Kumari *et al.* as a building block for an MIR trace gas sensor [139]. They theoretically investigated this structure as a sensor to detect NH_3 gas, and showed the detection down to 5 ppm using a ~8.7 mm-long device.

B. Silicon-on-Calcium-Fluoride

Calcium fluoride (CaF_2) is transparent in the spectral range from the visible, the NIR, to the MIR wavelength of $\lambda = 8$ μm, and possesses a low refractive index of ~1.4 over the entire region. Therefore, silicon-on-calcium-fluoride (SOCF) offers both a broad transparent window and the highest index contrast. The SOCF substrate was first experimentally investigated in 2014 by Chen *et al.* [140]. As shown in Figs. 21(a)–21(f), silicon waveguides and microring resonators were first patterned in an SOI substrate. After that, a polydimethylsiloxane (PDMS) stamp was used to peel off the patterned silicon membrane from the substrate. The PDMS was then pressed on a CaF_2 substrate and slowly removed. The patterned silicon membrane was bonded on a CaF_2 substrate by surface force. Figures 21(g)–21(i) show the fabricated silicon bus waveguide and a microring with a

Table 4. Summary of Devices on a Standard Silicon Wafer

Waveguide Types and Related Works	Propagation Loss (dB/cm)	Applications
Suspended-membrane-based waveguides [34]	4.0 dB/cm for TE at $\lambda = 3.39$ μm; 2.8 dB/cm for TM at $\lambda = 3.39$ μm [34]	N/A
T-guides [129]	1.75 dB/cm for TE at $\lambda = 3.64$ μm [129]	N/A
Pedestal waveguides [131,132]	2.7 dB/cm at $\lambda = 3.7$ μm [131]	Chemical sensing [132]
Silicon-on-porous-silicon (SiPSi) [60]	3.9 dB/cm for both TE and TM at $\lambda = 3.39$ μm [60]	N/A

60-μm radius on CaF_2 substrate. Edge coupling was used to couple light into and out from the device. The microring resonator had an intrinsic quality factor of 62,000 at $\lambda = 5.2$–μm wavelength, which corresponded to 3.8 dB/cm propagation loss. The application of this device for on-chip cavity-enhanced spectroscopy was also experimentally demonstrated by measuring the transmittance of the device immersed in a mixture of ethanol and toluene in cyclohexane as shown in Figs. 21(j)–21(l). Different concentration ratios between ethanol and toluene caused different refractive index changes (Δn) and absorption coefficients (α) of the mixture, leading to a change of the resonance peak wavelength and extinction ratio, respectively. Therefore, concentrations of ethanol and toluene were calculated using linear transformation. Low mass loading limits of detection of 0.05 ng for ethanol, 0.06 ng for toluene, and 0.09 ng for isopropyl alcohol were also demonstrated.

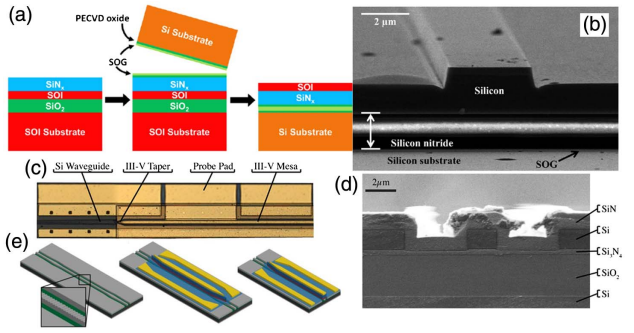

Fig. 20. Silicon-on-nitride (SON). (a) Schematic of the SON fabrication process [135]. (b) SEM image of the facet of a fabricated silicon waveguide on silicon nitride [135]. (c) Microscope image of an integrated QCL on SONOI platform [137]. (d) Facet of an integrated QCL on SONOI platform [137]. (e) Schematic of an integrated DFB QCL on SONOI. An SONOI waveguide with surface DFB grating (left panel). A DFB QCL is heterogeneously integrated with an SONOI waveguide (middle panel). One taper of the fabricated DFB QCL is removed (right panel) [138]. Figures are reproduced from: (a) and (b) Ref. [135]; (c) and (d) Ref. [137]; (e) Ref. [138].

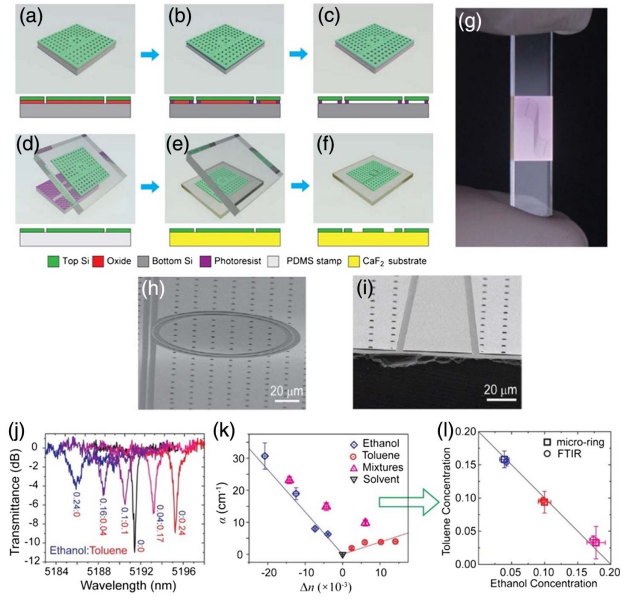

Fig. 21. Silicon-on-calcium-fluoride. (a)–(f) Schematic of the device fabrication process, showing a silicon membrane is transferred to a CaF_2 substrate. (g) Image of a fabricated silicon device (light purple) on CaF_2 (transparent). SEM images of (h) a silicon microring resonator on CaF_2 and (i) a taper at the edge of the chip for light coupling. (j) Measured transmittance of a fabricated microring immersed in different concentration ratios of ethanol and toluene in a cyclohexane mixture. (k) Derived absorption coefficient (α) and refractive index change (Δn) of the mixture from the measured extinction ratio and resonance peak shift in (j). Calibration samples of ethanol, toluene, and blank solvent are plotted. (l) Calculated concentrations of ethanol and toluene from (k) using linear transformation showing good agreement with FTIR data. Figures are reproduced from Ref. [140].

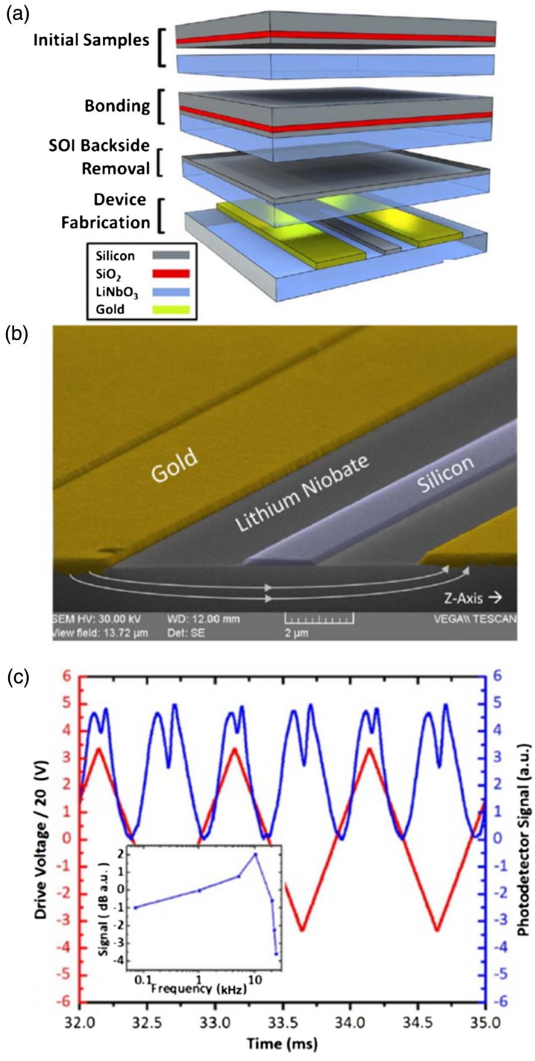

Fig. 22. Silicon-on-lithium-niobate. (a) Fabrication process for a silicon-on-lithium-niobate chip and the electro-optic modulators on it. (b) SEM image of a fabricated modulator in a silicon-on-lithium-niobate substrate. The applied field will follow the direction shown in white lines. (c) Modulator response (blue) in the time domain. The red line represents the drive voltage divided by 20. The inset shows the modulator response in the frequency domain. Figures are reproduced from Ref. [141].

Table 5. Summary for SON, SOCF, and SOLN

Platform and Published Works	Demonstrated Devices	Propagation Loss (dB/cm)	Best Reported Application Performance
Silicon-on-nitride (SON) [134,135,137–139]	Waveguide and hybrid QCL	TE: 5.2–0.6 dB/cm TM: 5.1–0.6 dB/cm at $\lambda = 3.39$ μm [135]	FP laser: 31 mW at 4.8 μm, at 20°C [137]; DFB laser: spanning 4.62–4.86 μm, 211 mW [138]
Silicon-on-calcium-fluoride (SOCF) [140]	Waveguide and ring resonator based sensor	3.8 dB/cm at $\lambda = 5.2$ μm [140]	$Q \sim 62,000$; mass LOD: 0.05 ng (ethanol), 0.06 ng (toluene), and 0.09 ng (IPA) [140]
Silicon-on-lithium-niobate (SOLN) [141]	Waveguide and EO modulator	2.5 dB/cm at $\lambda = 3.39$ μm [141]	$V\pi \cdot L = 26$ V · cm at 1 kHz; highest response shown in paper: 23 kHz [141]

Table 6. Comparison of MIR Silicon Platforms

Platforms	Pros	Cons
SOI	Most mature platform with commercially available substrate and standard fabrication process; high index contrast	Smallest bandwidth ($\lambda = 1.1$–3.8 μm); free-standing structures on SOI expand the bandwidth, but introduce fragile geometry and extra processing steps
SOS	Relatively mature platform with commercially available substrate; similar fabrication process; high index contrast	Limited bandwidth ($\lambda = 1.1$–5.5 μm); pure sapphire substrate brings some difficulties during e-beam exposure; extra loss from inherent twinning defects
Standard silicon wafer	Commercially available wafer, bandwidth as wide as silicon ($\lambda = 1.1$–8 μm)	Requires nonstandard processing to create vertical index contrast, such as free-standing configuration (mechanical instability), a supporting pedestal (complicates the fabrication process), or porous bottom cladding (scattering loss)
SON	Wide bandwidth ($\lambda = 1.1$–6.7 μm)	Requires wafer bonding
SOCF	Wide bandwidth covering the whole transparent window of silicon ($\lambda = 1.1$–8 μm)	Requires membrane transferring
SOLN	Possesses EO effect for active applications	Requires wafer bonding, limited bandwidth ($\lambda = 1.1$–5 μm)

C. Silicon-on-Lithium-Niobate

The lack of a dipolar second-order susceptibility ($\chi^{(2)}$) in silicon due to its centro-symmetric lattice is one major bottleneck of silicon photonics, usually limiting the usage of silicon in active device applications. Especially in MIR, a "greater-than-linear" increase of free-carrier absorption versus wavelength results in the dramatic loss increment that impedes applying plasma-dispersion-based techniques, which achieves great success for building silicon EO modulators in NIR to silicon modulators in MIR [142]. Thus, so far, the demonstrated longest operating wavelength of a silicon EO modulator is around $\lambda = 2$ μm [37]. On the other hand, lithium niobate ($LiNbO_3$) possesses strong EO coefficient, low refractive index (~2.1) and a broad transparency window from $\lambda = 350$ nm to 5 μm. The SOLN platform can thus combine all advantages from these two materials. In 2014, Chiles *et al.* experimentally demonstrated the first waveguide-type EO modulator in SOLN in MIR [141]. The SOLN substrate was produced through a wafer-bonding technique, as shown in Fig. 22(a). The optical waveguides show 2.5 dB/cm propagation loss for the TE mode at $\lambda = 3.39$ μm wavelength on this platform. MZI modulators [Fig. 22(b)], were fabricated and characterized at $\lambda = 3.39$ μm wavelength, showing extinction ratio of ~8 dB, a half-wave voltage-length product ($V_\pi \cdot L$) of 26 V·cm at 1 kHz [Fig. 22(c)], and an on-chip insertion loss of 3.3 dB. Owing to the limit of the photodetector's bandwidth, the measured highest frequency response of the modulators (inset of Fig. 22(c)] was 23 kHz.

The summary for three platforms in this section is shown in the following Table 5, covering most aspects of these three platforms and showing great potential for more functional MIR applications.

6. CONCLUSION

In summary, we have reviewed most of the recent advances in MIR silicon photonics on different platforms. Various fundamental photonic components including SWG couplers, single-mode strip waveguides, rib waveguides, slot waveguides, ring resonators, MZIs, AWGs, PCGs, PCs, PCWs, and MMIs, etc., on different platforms were discussed. We also discussed the applications of these devices as sensors, modulators, and photodetectors. Alongside the conventional platforms, several newly emerging complementary platforms, involving SON, SOCF, SOLN, SiPSi, and suspended-membrane- and SWG-based free-standing platforms, all promise to positively impact MIR silicon photonics. Significant efforts have been put on replacing buried oxide bottom cladding, on increasing operating bandwidth or providing new functions, and on reducing propagation loss. We provide comparison of all the platforms discussed in this paper as listed in Table 6.

As we may see from Table 6, each platform possesses its own pros and cons, which determine the applications. In general, we see an outlook of three directions for MIR silicon photonics applications.

A. On-Chip Sensing Systems

As discussed in the introduction section, MIR covers a so-called "molecular fingerprints" region that may facilitate MIR spectroscopic sensor development. Even though the transparency window of silicon is limited to 8 μm, considering the advantages silicon platform can offer, a silicon-based on-chip spectroscopic sensor is still highly desired. There are several areas requiring further exploration.

A. Promising device-performance improvement, such as reducing propagation loss, insertion loss, increasing quality factor, etc., will facilitate denser integration, more robust and more practical device demonstrations in existing platforms.

B. Extending the working bandwidth towards longer wavelength. Using a thicker silicon core to avoid too much interaction between light and the absorptive bottom cladding may be an approach, but it may also sacrifice the device sensitivity, and therefore better waveguide engineering is needed to balance these factors. On the perspective of the platform, the SOCF platform seems to cover the widest working range, but demonstrations of wavelength longer than 5.2 μm are lacking. Further fabrication improvement on this platform is also needed for more practical applications. Besides, other hybrid material platforms, such as germanium-on-silicon and silicon germanium-on-silicon, are also good candidates.

C. Monolithic integration of light source and photodetector. This is a very important step for a portable on-chip sensor. To fully utilize the bandwidth of silicon, a strong and wide band source is desired. Integrating a III/V DFB laser array on a silicon waveguide may solve this issue, but the tunability and covering range as well as the output power require further exploration. Nonlinear effects, such as stimulated Raman scattering and supercontinuum generation, may provide the other potential solution. High performance integrated photodetectors for longer wavelengths are still missing. Integrating quantum cascaded detectors and generating or converting frequency to short wavelengths using nonlinear effects might be potential approaches.

B. Optical Communications

MIR possesses two atmospheric transmission windows (3–5 μm and 8–12 μm), thus offering a new spectrum for transmitting light through free space. Especially, the 3–5 μm window is fully within the transparency window of silicon. Several existing platforms, such as SOS, standard silicon wafer, SON, SOCF, and SOLN cover the whole 3–5 μm window. Compared with NIR, MIR is more eye-safe and has a higher fabrication tolerance. However, several challenges need to be overcome.

A. Developing MIR modulators. A high-speed, low-loss, power-efficient MIR modulator is a key device for optical communications. The widely used modulator technology in NIR, free-carrier density modulation, has only been demonstrated at shorter wavelengths in the MIR. Extending its working wavelength to longer wavelengths is a challenge due to the dramatic increase of free-carrier absorption. On the other hand, using the greatly enhanced free-carrier absorption to build electroabsorption modulators may become a potential technology for modulating light in the MIR.

B. Pushing emerging platforms, such as SOLN, towards maturity may provide new directions for MIR silicon PIC development, since they provide more opportunities for optical communication applications.

C. Same as with on-chip sensing systems, device-performance improvement, light source, and photodetector integration require more investigations.

C. Nonlinear Photonics Lab-on-a-Chip

Nonlinear effects may play an important role in future MIR photonics research for potential applications in highly efficient MIR signal detection, ultrafast signal processing in all optical domains, as well as on-chip quantum interference. The strong optical confinement of silicon waveguides and negligible two-photon absorption when wavelengths are longer than 2.2 μm will facilitate nonlinearity device demonstrations on an MIR silicon platform, which potentially could be applied to solving light source and optical detection issues, monitoring the environment, imaging night-vision, and medical diagnostics.

Funding. National Natural Science Foundation of China (NSFC) (61705099); Natural Science Foundation of Jiangsu Province, China (BK20160631); National Science Foundation (NSF) (IIP-1127251); U.S. Army (W911SR-12-C-004); National Institute of Standards and Technology (NIST) (70NANB16H183); National Aeronautics and Space Administration (NASA) (NNX17CA44P).

Acknowledgment. S. Chakravarty and R. T. Chen also acknowledge NIST SBIR and NASA SBIR.

REFERENCES

1. A. Schliesser, N. Picqué, and T. W. Hänsch, "Mid-infrared frequency combs," Nat. Photonics **6**, 440–449 (2012).
2. R. Maulini, I. Dunayevskiy, A. Lyakh, A. Tsekoun, C. K. N. Patel, L. Diehl, C. Pflugl, and F. Capasso, "Widely tunable high-power external cavity quantum cascade laser operating in continuous-wave at room temperature," Electron. Lett. **45**, 107–108 (2009).
3. http://www.mksinst.com/product/.
4. http://www.tdlas.com/index.shtml.
5. http://www.tigeroptics.com/technology.html#cavity-ring-down-spectroscopy.
6. http://www.gasera.fi/technology/photoacoustics/solid-phase-pas/.
7. N. Hô, M. C. Phillips, H. Qiao, P. J. Allen, K. Krishnaswami, B. J. Riley, T. L. Myers, and N. C. Anheier, Jr., "Single-mode low-loss chalcogenide glass waveguides for the mid-infrared," Opt. Lett. **31**, 1860–1862 (2006).
8. C. Tsay, E. Mujagić, C. K. Madsen, C. F. Gmachl, and C. B. Arnold, "Mid-infrared characterization of solution-processed As_2S_3 chalcogenide glass waveguides," Opt. Express **18**, 15523–15530 (2010).
9. P. Ma, D.-Y. Choi, Y. Yu, X. Gai, Z. Yang, S. Debbarma, S. Madden, and B. Luther-Davies, "Low-loss chalcogenide waveguides for chemical sensing in the mid-infrared," Opt. Express **21**, 29927–29937 (2013).
10. O. Eyal, V. Scharf, S. Shalem, and A. Katzir, "Single-mode mid-infrared silver halide planar waveguides," Opt. Lett. **21**, 1147–1149 (1996).
11. B. Dekel and A. Katzir, "Silver halide planar waveguides and grating couplers for middle infrared integrated optics," Appl. Phys. Lett. **97**, 241106 (2010).
12. T. Lewi and A. Katzir, "Silver halide single-mode strip waveguides for the mid-infrared," Opt. Lett. **37**, 2733–2735 (2012).
13. P. T. Lin, V. Singh, L. Kimerling, and A. M. Agarwal, "Planar silicon nitride mid-infrared devices," Appl. Phys. Lett. **102**, 251121 (2013).
14. K. Luke, Y. Okawachi, M. R. E. Lamont, A. L. Gaeta, and M. Lipson, "Broadband mid-infrared frequency comb generation in a Si_3N_4 microresonator," Opt. Lett. **40**, 4823–4826 (2015).

15. T. Hu, B. Dong, X. Luo, T.-Y. Liow, J. Song, C. Lee, and G.-Q. Lo, "Silicon photonic platforms for mid-infrared applications [Invited]," Photon. Res. **5**, 417–430 (2017).
16. C. Charlton, M. Giovannini, J. Faist, and B. Mizaikoff, "Fabrication and characterization of molecular beam epitaxy grown thin-film GaAs waveguides for mid-infrared evanescent field chemical sensing," Anal. Chem. **78**, 4224–4227 (2006).
17. M. Sieger, F. Balluff, X. Wang, S.-S. Kim, L. Leidner, G. Gauglitz, and B. Mizaikoff, "On-chip integrated mid-infrared GaAs/AlGaAs Mach-Zehnder interferometer," Anal. Chem. **85**, 3050–3052 (2013).
18. X. Wang, S.-S. Kim, R. Roßbach, M. Jetter, P. Michler, and B. Mizaikoff, "Ultra-sensitive mid-infrared evanescent field sensors combining thin-film strip waveguides with quantum cascade lasers," Analyst **137**, 2322–2327 (2012).
19. P. T. Lin, H. Jung, L. C. Kimerling, A. Agarwal, and H. X. Tang, "Low-loss aluminium nitride thin film for mid-infrared microphotonics," Laser Photon. Rev. **8**, L23–L28 (2014).
20. X. Wang, J. Antoszewski, G. Putrino, W. Lei, L. Faraone, and B. Mizaikoff, "Mercury-cadmium–telluride waveguides-a novel strategy for on-chip mid-infrared sensors," Anal. Chem. **85**, 10648–10652 (2013).
21. J. Cardenas, M. Yu, Y. Okawachi, C. B. Poitras, R. K. Lau, A. Dutt, A. L. Gaeta, and M. Lipson, "Optical nonlinearities in high-confinement silicon carbide waveguides," Opt. Lett. **40**, 4138–4141 (2015).
22. Y. C. Chang, V. Paeder, L. Hvozdara, J. M. Hartmann, and H. P. Herzig, "Low-loss germanium strip waveguides on silicon for the mid-infrared," Opt. Lett. **37**, 2883–2885 (2012).
23. A. Malik, M. Muneeb, S. Pathak, Y. Shimura, J. Van Campenhout, R. Loo, and G. Roelkens, "Germanium-on-silicon mid-infrared arrayed waveguide grating multiplexers," IEEE Photon. Technol. Lett. **25**, 1805–1808 (2013).
24. A. Malik, M. Muneeb, Y. Shimura, J. Van Campenhout, R. Loo, and G. Roelkens, "Germanium-on-silicon planar concave grating wavelength (de) multiplexers in the mid-infrared," Appl. Phys. Lett. **103**, 161119 (2013).
25. A. Malik, M. Muneeb, Y. Shimura, J. Van Campenhout, and G. Roelkens, "Germanium-on-silicon mid-infrared waveguides and Mach-Zehnder interferometers," in *IEEE Photonics Conference* (2013).
26. J. Kang, M. Takenaka, and S. Takagi, "Novel Ge waveguide platform on Ge-on-insulator wafer for mid-infrared photonic integrated circuits," Opt. Express **24**, 11855–11864 (2016).
27. G. Mashanovich, C. Mitchell, J. Soler Penades, A. Khokhar, C. Littlejohns, W. Cao, Z. Qu, S. Stankovic, F. Gardes, and T. B. Masaud, "Germanium mid-infrared photonic devices," J. Lightwave Technol. **35**, 624–630 (2017).
28. U. Younis, S. K. Vanga, A. E.-J. Lim, P. G.-Q. Lo, A. A. Bettiol, and K.-W. Ang, "Germanium-on-SOI waveguides for mid-infrared wavelengths," Opt. Express **24**, 11987–11993 (2016).
29. A. Bogris, A. Kapsalis, K. Hammani, M. A. Ettabib, M. Brun, P. Labeye, S. Nicoletti, P. Petropoulos, and D. Syvridis, "Silicon germanium platform enabling mid-infrared to near-infrared conversion for telecom and sensing applications," in *European Conference on Optical Communication (ECOC)* (2014).
30. M. Brun, P. Labeye, G. Grand, J.-M. Hartmann, F. Boulila, M. Carras, and S. Nicoletti, "Low loss SiGe graded index waveguides for mid-IR applications," Opt. Express **22**, 508–518 (2014).
31. L. Carletti, P. Ma, B. Luther-Davies, D. D. Hudson, C. Monat, S. Madden, D. J. Moss, M. Brun, S. Ortiz, and S. Nicoletti, "Nonlinear optical properties of SiGe waveguides in the mid-infrared," in *CLEO: Science and Innovations* (Optical Society of America, 2014), paper SW3M.7.
32. L. Carletti, D. Allioux, P. Ma, Y. Yu, B. Luther-Davies, S. Madden, D. Hudson, M. Sinobad, D. Moss, and M. Brun, "Mid-infrared nonlinear optics in SiGe waveguides," in *Summer Topical Meeting Series (SUM)* (IEEE, 2015), pp. 59–60.
33. R. Soref, "Mid-infrared photonics in silicon and germanium," Nat. Photonics **4**, 495–497 (2010).
34. J. Chiles, S. Khan, J. Ma, and S. Fathpour, "High-contrast, all-silicon waveguiding platform for ultra-broadband mid-infrared photonics," Appl. Phys. Lett. **103**, 151106 (2013).
35. J. Soler Penades, C. Alonso-Ramos, A. Khokhar, M. Nedeljkovic, L. Boodhoo, A. Ortega-Moñux, I. Molina-Fernández, P. Cheben, and G. Mashanovich, "Suspended SOI waveguide with sub-wavelength grating cladding for mid-infrared," Opt. Lett. **39**, 5661–5664 (2014).
36. M. Nedeljkovic, S. Stankovic, C. J. Mitchell, A. Z. Khokhar, S. A. Reynolds, D. J. Thomson, F. Y. Gardes, C. G. Littlejohns, G. T. Reed, and G. Z. Mashanovich, "Mid-infrared thermo-optic modulators in SoI," IEEE Photon. Technol. Lett. **26**, 1352–1355 (2014).
37. M. A. Van Camp, S. Assefa, D. M. Gill, T. Barwicz, S. M. Shank, P. M. Rice, T. Topuria, and W. M. Green, "Demonstration of electrooptic modulation at 2165 nm using a silicon Mach-Zehnder interferometer," Opt. Express **20**, 28009–28016 (2012).
38. J. J. Ackert, D. J. Thomson, L. Shen, A. C. Peacock, P. E. Jessop, G. T. Reed, G. Z. Mashanovich, and A. P. Knights, "High-speed detection at two micrometres with monolithic silicon photodiodes," Nat. Photonics **9**, 393–396 (2015).
39. M. Muneeb, X. Chen, P. Verheyen, G. Lepage, S. Pathak, E. Ryckeboer, A. Malik, B. Kuyken, M. Nedeljkovic, and J. Van Campenhout, "Demonstration of silicon-on-insulator mid-infrared spectrometers operating at 3.8 μm," Opt. Express **21**, 11659–11669 (2013).
40. E. Ryckeboer, A. Gassenq, M. Muneeb, N. Hattasan, S. Pathak, L. Cerutti, J. B. Rodriguez, E. Tournié, W. Bogaerts, R. Baets, and G. Roelkens, "Silicon-on-insulator spectrometers with integrated GaInAsSb photodiodes for wide-band spectroscopy from 1510 to 2300 nm," Opt. Express **21**, 6101–6108 (2013).
41. M. Nedeljkovic, A. V. Velasco, A. Z. Khokhar, A. Delâge, P. Cheben, and G. Z. Mashanovich, "Mid-infrared silicon-on-insulator Fourier-transform spectrometer chip," IEEE Photon. Technol. Lett. **28**, 528–531 (2016).
42. S. Zlatanovic, J. S. Park, S. Moro, J. M. C. Boggio, I. B. Divliansky, A. Nikola, S. Mookherjea, and S. Radic, "Mid-infrared wavelength conversion in silicon waveguides using ultracompact telecom-band-derived pump source," Nat. Photonics **4**, 561–564 (2010).
43. A. G. Griffith, R. K. Lau, J. Cardenas, Y. Okawachi, A. Mohanty, R. Fain, Y. H. D. Lee, M. Yu, C. T. Phare, and C. B. Poitras, "Silicon-chip mid-infrared frequency comb generation," Nat. Commun. **6**, 6299 (2015).
44. X. Liu, B. Kuyken, G. Roelkens, R. Baets, R. M. Osgood, and W. M. J. Green, "Bridging the mid-infrared-to-telecom gap with silicon nanophotonic spectral translation," Nat. Photonics **6**, 667–671 (2012).
45. B. Kuyken, X. Liu, R. M. Osgood, R. Baets, G. Roelkens, and W. M. J. Green, "Mid-infrared to telecom-band supercontinuum generation in highly nonlinear silicon-on-insulator wire waveguides," Opt. Express **19**, 20172–20181 (2011).
46. X. Liu, R. M. Osgood, Y. A. Vlasov, and W. M. J. Green, "Mid-infrared optical parametric amplifier using silicon nanophotonic waveguides," Nat. Photonics **4**, 557–560 (2010).
47. J. Huang, H. Han, A. Liu, H. Wang, X. Liu, Y. Zou, M.-H. Lu, and Y.-F. Chen, "Efficient second harmonic generation by mode phase matching in a silicon waveguide," IEEE Photon. J. **9**, 6100807 (2017).
48. E. Timurdogan, C. V. Poulton, M. Byrd, and M. Watts, "Electric field-induced second-order nonlinear optical effects in silicon waveguides," Nat. Photonics **11**, 200–206 (2017).
49. R. K. W. Lau, M. R. E. Lamont, A. G. Griffith, Y. Okawachi, M. Lipson, and A. L. Gaeta, "Octave-spanning mid-infrared supercontinuum generation in silicon nanowaveguides," Opt. Lett. **39**, 4518–4521 (2014).
50. A. G. Griffith, M. Yu, Y. Okawachi, J. Cardenas, A. Mohanty, A. L. Gaeta, and M. Lipson, "Coherent mid-infrared frequency combs in silicon-microresonators in the presence of Raman effects," Opt. Express **24**, 13044–13050 (2016).
51. M. Yu, Y. Okawachi, A. G. Griffith, M. Lipson, and A. L. Gaeta, "Mode-locked mid-infrared frequency combs in a silicon microresonator," Optica **3**, 854–860 (2016).
52. R. Shankar and M. Lončar, "Silicon photonic devices for mid-infrared applications," Nanophotonics **3**, 329–341 (2014).
53. V. Singh, P. T. Lin, N. Patel, H. Lin, L. Li, Y. Zou, F. Deng, C. Ni, J. Hu, and J. Giammarco, "Mid-infrared materials and devices on a

Si platform for optical sensing," Sci. Technol. Adv. Mater. **15**, 014603 (2014).
54. G. Z. Mashanovich, F. Y. Gardes, D. J. Thomson, Y. Hu, K. Li, M. Nedeljkovic, J. Soler Penades, A. Z. Khokhar, C. J. Mitchell, and S. Stankovic, "Silicon photonic waveguides and devices for near-and mid-IR applications," IEEE J. Sel. Top. Quantum Electron. **21**, 407–418 (2015).
55. M. Nedeljkovic, A. Khokhar, Y. Hu, X. Chen, J. Soler Penades, S. Stankovic, H. Chong, D. Thomson, F. Gardes, and G. Reed, "Silicon photonic devices and platforms for the mid-infrared," Opt. Mater. Express **3**, 1205–1214 (2013).
56. G. Roelkens, U. Dave, A. Gassenq, N. Hattasan, C. Hu, B. Kuyken, F. Leo, A. Malik, M. Muneeb, E. Ryckeboer, S. Uvin, Z. Hens, R. Baets, Y. Shimura, F. Gencarelli, B. Vincent, R. Loo, J. Van Campenhout, L. Cerutti, J.-B. Rodriguez, E. Tournié, X. Chen, M. Nedeljkovic, G. Mashanovich, L. Shen, N. Healy, A. C. Peacock, X. Liu, R. Osgood, and W. Green, "Silicon-based heterogeneous photonic integrated circuits for the mid-infrared," Opt. Mater. Express **3**, 1523–1536 (2013).
57. N. Hattasan, B. Kuyken, F. Leo, E. M. P. Ryckeboer, D. Vermeulen, and G. Roelkens, "High-efficiency SOI fiber-to-chip grating couplers and low-loss waveguides for the short-wave infrared," IEEE Photon. Technol. Lett. **24**, 1536–1538 (2012).
58. F. Leo, B. Kuyken, N. Hattasan, R. Baets, and G. Roelkens, "Passive SOI devices for the short-wave-infrared," in *16th European Conference on Integrated Optics (ECIO)* (2012).
59. M. S. Rouifed, C. G. Littlejohns, G. X. Tina, H. Qiu, J. Soler Penades, M. Nedeljkovic, Z. Zhang, C. Liu, D. J. Thomson, G. Z. Mashanovich, G. T. Reed, and H. Wang, "Ultra-compact MMI-based beam splitter demultiplexer for the NIR/MIR wavelengths of 1.55 μm and 2 μm," Opt. Express **25**, 10893–10900 (2017).
60. G. Z. Mashanovich, M. M. Milošević, M. Nedeljkovic, N. Owens, B. Xiong, E. J. Teo, and Y. Hu, "Low loss silicon waveguides for the mid-infrared," Opt. Express **19**, 7112–7119 (2011).
61. M. M. Milosevic, M. Nedeljkovic, T. M. B. Masaud, E. Jaberansary, H. M. H. Chong, N. G. Emerson, G. T. Reed, and G. Z. Mashanovich, "Silicon waveguides and devices for the mid-infrared," Appl. Phys. Lett. **101**, 121105 (2012).
62. J. Soler Penades, A. Z. Khokhar, M. Nedeljkovic, and G. Z. Mashanovich, "Low loss mid-infrared SOI slot waveguides," IEEE Photon. Technol. Lett. **27**, 1197–1199 (2015).
63. B. Dong, X. Guo, C. P. Ho, B. Li, H. Wang, C. Lee, X. Luo, and G.-Q. Lo, "Silicon-on-insulator waveguide devices for broadband mid-infrared photonics," IEEE Photon. J. **9**, 4501410 (2017).
64. P. T. Lin, S. W. Kwok, H.-Y. G. Lin, V. Singh, L. C. Kimerling, G. M. Whitesides, and A. Agarwal, "Mid-infrared spectrometer using opto-nanofluidic slot-waveguide for label-free on-chip chemical sensing," Nano Lett. **14**, 231–238 (2013).
65. Y. Wei, G. Li, Y. Hao, Y. Li, J. Yang, M. Wang, and X. Jiang, "Long-wave infrared 1 × 2 MMI based on air-gap beneath silicon rib waveguides," Opt. Express **19**, 15803–15809 (2011).
66. M. Florjańczyk, P. Cheben, S. Janz, A. Scott, B. Solheim, and D.-X. Xu, "Multiaperture planar waveguide spectrometer formed by arrayed Mach-Zehnder interferometers," Opt. Express **15**, 18176–18189 (2007).
67. B. Troia, A. Z. Khokhar, M. Nedeljkovic, J. Soler Penades, V. M. Passaro, and G. Z. Mashanovich, "Cascade-coupled racetrack resonators based on the Vernier effect in the mid-infrared," Opt. Express **22**, 23990–24003 (2014).
68. Y. Hu, T. Li, D. J. Thomson, X. Chen, J. Soler Penades, A. Z. Khokhar, C. J. Mitchell, G. T. Reed, and G. Z. Mashanovich, "Mid-infrared wavelength division (de)multiplexer using an interleaved angled multimode interferometer on the silicon-on-insulator platform," Opt. Lett. **39**, 1406–1409 (2014).
69. R. Wang, S. Sprengel, G. Boehm, R. Baets, M.-C. Amann, and G. Roelkens, "Broad wavelength coverage 2.3 μm III-V-on-silicon DFB laser array," Optica **4**, 972–975 (2017).
70. P. Dong, T.-C. Hu, L. Zhang, M. Dinu, R. Kopf, A. Tate, L. Buhl, D. Neilson, X. Luo, and T.-Y. Liow, "1.9 μm hybrid silicon/III-V semiconductor laser," Electron. Lett. **49**, 664–666 (2013).
71. G. Roelkens, U. D. Dave, A. Gassenq, N. Hattasan, C. Hu, B. Kuyken, F. Leo, A. Malik, M. Muneeb, E. Ryckeboer, D. Sanchez, S. Uvin, R. Wang, Z. Hens, R. Baets, Y. Shimura, F. Gencarelli, B. Vincent, R. Loo, J. V. Campenhout, L. Cerutti, J. B. Rodriguez, E. Tournié, X. Chen, M. Nedeljkovic, G. Mashanovich, L. Shen, N. Healy, A. C. Peacock, X. Liu, R. Osgood, and W. M. J. Green, "Silicon-based photonic integration beyond the telecommunication wavelength range," IEEE J. Sel. Top. Quantum Electron. **20**, 394–404 (2014).
72. A. Spott, M. Davenport, J. Peters, J. Bovington, M. J. R. Heck, E. J. Stanton, I. Vurgaftman, J. Meyer, and J. Bowers, "Heterogeneously integrated 2.0 μm CW hybrid silicon lasers at room temperature," Opt. Lett. **40**, 1480–1483 (2015).
73. R. Wang, S. Sprengel, G. Boehm, M. Muneeb, R. Baets, M.-C. Amann, and G. Roelkens, "2.3 μm range InP-based type-II quantum well Fabry-Perot lasers heterogeneously integrated on a silicon photonic integrated circuit," Opt. Express **24**, 21081–21089 (2016).
74. R. Wang, S. Sprengel, A. Malik, A. Vasiliev, G. Boehm, R. Baets, M.-C. Amann, and G. Roelkens, "Heterogeneously integrated III-V-on-silicon 2.3x μm distributed feedback lasers based on a type-II active region," Appl. Phys. Lett. **109**, 221111 (2016).
75. M. Muneeb, A. Ruocco, A. Malik, S. Pathak, E. Ryckeboer, D. Sanchez, L. Cerutti, J. B. Rodriguez, E. Tournié, W. Bogaerts, M. K. Smit, and G. Roelkens, "Silicon-on-insulator shortwave infrared wavelength meter with integrated photodiodes for on-chip laser monitoring," Opt. Express **22**, 27300–27308 (2014).
76. R. Wang, S. Sprengel, M. Muneeb, G. Boehm, R. Baets, M.-C. Amann, and G. Roelkens, "2 μm wavelength range InP-based type-II quantum well photodiodes heterogeneously integrated on silicon photonic integrated circuits," Opt. Express **23**, 26834–26841 (2015).
77. Z. Cheng, X. Chen, C. Wong, K. Xu, C. K. Fung, Y. Chen, and H. K. Tsang, "Focusing subwavelength grating coupler for mid-infrared suspended membrane waveguide," Opt. Lett. **37**, 1217–1219 (2012).
78. Z. Cheng, X. Chen, C. Y. Wong, K. Xu, and H. Tsang, "Mid-infrared suspended membrane waveguide and ring resonator on silicon-on-insulator," IEEE Photon. J. **4**, 1510–1519 (2012).
79. Y. A. Vlasov, M. O'Boyle, H. F. Hamann, and S. J. McNab, "Active control of slow light on a chip with photonic crystal waveguides," Nature **438**, 65–69 (2005).
80. Y. Akahane, T. Asano, B. S. Song, and S. Noda, "High-Q photonic nanocavity in a two-dimensional photonic crystal," Nature **425**, 944–947 (2003).
81. A. Vasiliev, A. Malik, M. Muneeb, B. Kuyken, R. Baets, and G. N. Roelkens, "On-chip mid-infrared photothermal spectroscopy using suspended silicon-on-insulator microring resonators," ACS Sens. **1**, 1301–1307 (2016).
82. X. Wang, Z. Cheng, K. Xu, H. K. Tsang, and J.-B. Xu, "High-responsivity graphene/silicon-heterostructure waveguide photodetectors," Nat. Photonics **7**, 888–891 (2013).
83. Y. Xia, C. Qiu, X. Zhang, W. Gao, J. Shu, and Q. Xu, "Suspended Si ring resonator for mid-IR application," Opt. Lett. **38**, 1122–1124. (2013).
84. S. Miller, A. Griffith, M. Yu, A. L. Gaeta, and M. Lipson, "Low-loss air-clad suspended silicon platform for mid-infrared photonics," in *CLEO: Science and Innovations* (Optical Society of America, 2016), paper STu3Q.6.
85. E. Yablonovitch, "Inhibited spontaneous emission in solid-state physics and electronics," Phys. Rev. Lett. **58**, 2059–2062 (1987).
86. S. John, "Strong localization of photons in certain disordered dielectric superlattices," Phys. Rev. Lett. **58**, 2486–2489 (1987).
87. R. Shankar, I. Bulu, R. Leijssen, and M. Lončar, "Study of thermally-induced optical bistability and the role of surface treatments in Si-based mid-infrared photonic crystal cavities," Opt. Express **19**, 24828–24837 (2011).
88. R. Shankar, R. Leijssen, I. Bulu, and M. Lončar, "Mid-infrared photonic crystal cavities in silicon," Opt. Express **19**, 5579–5586 (2011).
89. C. Reimer, M. Nedeljkovic, D. J. Stothard, M. O. Esnault, C. Reardon, L. O'Faolain, M. Dunn, G. Z. Mashanovich, and T. F. Krauss, "Mid-infrared photonic crystal waveguides in silicon," Opt. Express **20**, 29361–29368 (2012).

90. P. Cheben, P. J. Bock, J. H. Schmid, J. Lapointe, S. Janz, D.-X. Xu, A. Densmore, A. Delâge, B. Lamontagne, and T. J. Hall, "Refractive index engineering with subwavelength gratings for efficient microphotonic couplers and planar waveguide multiplexers," Opt. Lett. **35**, 2526–2528 (2010).
91. J. Schmid, P. Cheben, P. Bock, R. Halir, J. Lapointe, S. Janz, A. Dela, A. Densmore, J.-M. Fedeli, and T. Hall, "Refractive index engineering with subwavelength gratings in silicon microphotonic waveguides," IEEE Photon. J. **3**, 597–607 (2011).
92. X. Chen, K. Xu, Z. Cheng, C. K. Y. Fung, and H. K. Tsang, "Wideband subwavelength gratings for coupling between silicon-on-insulator waveguides and optical fibers," Opt. Lett. **37**, 3483–3485 (2012).
93. X. Xu, H. Subbaraman, J. Covey, D. Kwong, A. Hosseini, and R. T. Chen, "Complementary metal–oxide–semiconductor compatible high efficiency subwavelength grating couplers for silicon integrated photonics," Appl. Phys. Lett. **101**, 031109 (2012).
94. J. Gonzalo Wangüemert-Pérez, P. Cheben, A. Ortega-Moñux, C. Alonso-Ramos, D. Pérez-Galacho, R. Halir, I. Molina-Fernández, D.-X. Xu, and J. H. Schmid, "Evanescent field waveguide sensing with subwavelength grating structures in silicon-on-insulator," Opt. Lett. **39**, 4442–4445 (2014).
95. R. Halir, A. Ortega-Monux, J. H. Schmid, C. Alonso-Ramos, J. Lapointe, D.-X. Xu, J. G. Wanguemert-Perez, I. Molina-Fernandez, and S. Janz, "Recent advances in silicon waveguide devices using sub-wavelength gratings," IEEE J. Sel. Top. Quantum Electron. **20**, 279–291 (2014).
96. J. Wang, I. Glesk, and L. R. Chen, "Subwavelength grating filtering devices," Opt. Express **22**, 15335–15345 (2014).
97. J. Soler Penades, A. Ortega-Moñux, M. Nedeljkovic, J. G. Wangüemert-Pérez, R. Halir, A. Z. Khokhar, C. Alonso-Ramos, Z. Qu, I. Molina-Fernández, P. Cheben, and G. Z. Mashanovich, "Suspended silicon mid-infrared waveguide devices with subwavelength grating metamaterial cladding," Opt. Express **24**, 22908–22916 (2016).
98. R. A. Johnson, P. R. D. L. Houssaye, C. E. Chang, C. Pin-Fan, M. E. Wood, G. A. Garcia, I. Lagnado, and P. M. Asbeck, "Advanced thin-film silicon-on-sapphire technology: microwave circuit applications," IEEE Trans. Electron. Devices **45**, 1047–1054 (1998).
99. G. Imthurn, "*The history of silicon-on-sapphire*," White Paper (Peregrine Semiconductor Corporation, 2007), https://pdfs.semanticscholar.org/3383/eb0297213d217c88723662c10d263b186a7b.pdf.
100. T. Baehr-Jones, A. Spott, R. Ilic, B. Penkov, W. Asher, and M. Hochberg, "Silicon-on-sapphire integrated waveguides for the mid-infrared," Opt. Express **18**, 12127–12135 (2010).
101. F. Li, S. D. Jackson, C. Grillet, E. Magi, D. Hudson, S. J. Madden, Y. Moghe, C. O'Brien, A. Read, and S. G. Duvall, "Low propagation loss silicon-on-sapphire waveguides for the mid-infrared," Opt. Express **19**, 15212–15220 (2011).
102. N. Singh, D. D. Hudson, Y. Yu, C. Grillet, S. D. Jackson, A. Casas-Bedoya, A. Read, P. Atanackovic, S. G. Duvall, and S. Palomba, "Midinfrared supercontinuum generation from 2 to 6 μm in a silicon nanowire," Optica **2**, 797–802 (2015).
103. Y. Zou, H. Subbaraman, S. Chakravarty, X. Xu, A. Hosseini, W.-C. Lai, P. Wray, and R. T. Chen, "Grating-coupled silicon-on-sapphire integrated slot waveguides operating at mid-infrared wavelengths," Opt. Lett. **39**, 3070–3073 (2014).
104. Y. Zou, S. Chakravarty, and R. T. Chen, "Mid-infrared silicon-on-sapphire waveguide coupled photonic crystal microcavities," Appl. Phys. Lett. **107**, 081109 (2015).
105. A. Spott, Y. Liu, T. Baehr-Jones, R. Ilic, and M. Hochberg, "Silicon waveguides and ring resonators at 5.5 mu m," Appl. Phys. Lett. **97**, 213501 (2010).
106. R. Shankar, I. Bulu, and M. Loncar, "Integrated high-quality factor silicon-on-sapphire ring resonators for the mid-infrared," Appl. Phys. Lett. **102**, 051108 (2013).
107. Z. Cheng, X. Chen, C. Wong, K. Xu, C. K. Fung, Y. Chen, and H. K. Tsang, "Mid-infrared grating couplers for silicon-on-sapphire waveguides," IEEE Photon. J. **4**, 104–113 (2012).
108. http://www.thorlabs.us/newgrouppage9.cfm?objectgroup_id=7062.
109. Y. Zou, S. Chakravarty, D. N. Kwong, W.-C. Lai, X. Xu, X. Lin, A. Hosseini, and R. T. Chen, "Cavity-waveguide coupling engineered high sensitivity silicon photonic crystal microcavity biosensors with high yield," IEEE J. Sel. Top. Quantum Electron. **20**, 171–180 (2014).
110. C. Y. Wong, Z. Cheng, X. Chen, K. Xu, C. K. Fung, Y. M. Chen, and H. K. Tsang, "Characterization of mid-infrared silicon-on-sapphire microring resonators with thermal tuning," IEEE Photon. J. **4**, 1095–1102 (2012).
111. W.-C. Lai, S. Chakravarty, Y. Zou, and R. T. Chen, "Multiplexed detection of xylene and trichloroethylene in water by photonic crystal absorption spectroscopy," Opt. Lett. **38**, 3799–3802 (2013).
112. Y. Zou, S. Chakravarty, P. Wray, and R. T. Chen, "Experimental demonstration of propagation characteristics of mid-infrared photonic crystal waveguides in silicon-on-sapphire," Opt. Express **23**, 6965–6975 (2015).
113. Y. Zou, S. Chakravarty, L. Zhu, and R. T. Chen, "The role of group index engineering in series-connected photonic crystal microcavities for high density sensor microarrays," Appl. Phys. Lett. **104**, 141103 (2014).
114. S. Chakravarty, Y. Zou, W.-C. Lai, and R. T. Chen, "Slow light engineering for high Q high sensitivity photonic crystal microcavity biosensors in silicon," Biosens. Bioelectron. **38**, 170–176 (2012).
115. Y. Zou, S. Chakravarty, P. Wray, and R. T. Chen, "Mid-infrared holey and slotted photonic crystal waveguides in silicon-on-sapphire for chemical warfare simulant detection," Sens. Actuators B **221**, 1094–1103 (2015).
116. W.-C. Lai, S. Chakravarty, Y. Zou, and R. T. Chen, "Silicon nanomembrane based photonic crystal microcavities for high sensitivity bio-sensing," Opt. Lett. **37**, 1208–1210 (2012).
117. Y. Zou, S. Chakravarty, W.-C. Lai, C.-Y. Lin, and R. T. Chen, "Methods to array photonic crystal microcavities for high throughput high sensitivity biosensing on a silicon-chip based platform," Lab Chip **12**, 2309–2312 (2012).
118. C. J. Smith, R. Shankar, M. Laderer, M. B. Frish, M. Loncar, and M. G. Allen, "Sensing nitrous oxide with QCL-coupled silicon-on-sapphire ring resonators," Opt. Express **23**, 5491–5499 (2015).
119. N. Singh, A. Casas-Bedoya, D. D. Hudson, A. Read, E. Mägi, and B. J. Eggleton, "Mid-IR absorption sensing of heavy water using a silicon-on-sapphire waveguide," Opt. Lett. **41**, 5776–5779 (2016).
120. G. M. Hale and M. R. Querry, "Optical constants of water in the 200-nm to 200-μm wavelength region," Appl. Opt. **12**, 555–563 (1973).
121. Y. Zou, S. Chakravarty, C.-J. Chung, and R. T. Chen, "Miniature mid-infrared thermooptic switch with photonic crystal waveguide based silicon-on-sapphire Mach-Zehnder interferometers," Proc. SPIE **9753**, 97530Q (2016).
122. M. Soljačić and J. D. Joannopoulos, "Enhancement of nonlinear effects using photonic crystals," Nat. Mater. **3**, 211–219 (2004).
123. N. Singh, D. D. Hudson, and B. J. Eggleton, "Silicon-on-sapphire pillar waveguides for mid-IR supercontinuum generation," Opt. Express **23**, 17345–17354 (2015).
124. Y. Huang, E. Tien, S. Gao, S. Kalyoncu, Q. Song, F. Qian, E. Adas, D. Yildirim, and O. Boyraz, "Electrical signal-to-noise ratio improvement in indirect detection of mid-IR signals by wavelength conversion in silicon-on-sapphire waveguides," Appl. Phys. Lett. **99**, 181122 (2011).
125. W. Zhaolu, L. Hongjun, H. Nan, S. Qibing, and L. Xuefeng, "Mid-infrared Raman amplification and wavelength conversion in dispersion engineered silicon-on-sapphire waveguides," J. Opt. **16**, 015206 (2014).
126. Z. Wang, H. Liu, N. Huang, Q. Sun, J. Wen, and X. Li, "Influence of three-photon absorption on mid-infrared cross-phase modulation in silicon-on-sapphire waveguides," Opt. Express **21**, 1840–1848 (2013).
127. C.-M. Chang and O. Solgaard, "Fano resonances in integrated silicon Bragg reflectors for sensing applications," Opt. Express **21**, 27209–27218 (2013).
128. G. Tittelbach, B. Richter, and W. Karthe, "Comparison of three transmission methods for integrated optical waveguide propagation loss measurement," J. Opt. Pure Appl. Opt. **2**, 683–700 (1993).

129. J. Chiles and S. Fathpour, "Single-mode and single-polarization photonics with anchored-membrane waveguides," Opt. Express **24**, 19337–19343 (2016).
130. C. M. Chang and O. Solgaard, "Monolithic silicon waveguides in standard silicon," IEEE Micro **33**, 32–40 (2013).
131. P. T. Lin, V. Singh, Y. Cai, L. C. Kimerling, and A. Agarwal, "Air-clad silicon pedestal structures for broadband mid-infrared microphotonics," Opt. Lett. **38**, 1031–1033 (2013).
132. P. T. Lin, V. Singh, J. Hu, K. Richardson, J. D. Musgraves, I. Luzinov, J. Hensley, L. C. Kimerling, and A. Agarwal, "Chip-scale mid-infrared chemical sensors using air-clad pedestal silicon waveguides," Lab Chip **13**, 2161–2166 (2013).
133. A. S. Richard, J. E. Stephen, and R. B. Walter, "Silicon waveguided components for the long-wave infrared region," J. Opt. A **8**, 840–848 (2006).
134. Y. Yue, L. Zhang, H. Huang, R. G. Beausoleil, and A. E. Willner, "Silicon-on-nitride waveguide with ultralow dispersion over an octave-spanning mid-infrared wavelength range," IEEE Photon. J. **4**, 126–132 (2012).
135. S. Khan, J. Chiles, J. Ma, and S. Fathpour, "Silicon-on-nitride waveguides for mid-and near-infrared integrated photonics," Appl. Phys. Lett. **102**, 121104 (2013).
136. G. Mashanovich, W. Headley, M. Milosevic, N. Owens, E. Teo, B. Xiong, P. Yang, M. Nedeljkovic, J. Anguita, and I. Marko, "Waveguides for mid-infrared group IV photonics," in *7th IEEE International Conference on Group IV Photonics (GFP)* (IEEE, 2010), pp. 374–376.
137. A. Spott, J. Peters, M. L. Davenport, E. J. Stanton, C. D. Merritt, W. W. Bewley, I. Vurgaftman, C. S. Kim, J. R. Meyer, J. Kirch, L. J. Mawst, D. Botez, and J. E. Bowers, "Quantum cascade laser on silicon," Optica **3**, 545–551 (2016).
138. A. Spott, J. Peters, M. Davenport, E. Stanton, C. Zhang, C. Merritt, W. Bewley, I. Vurgaftman, C. Kim, J. Meyer, J. Kirch, L. Mawst, D. Botez, and J. Bowers, "Heterogeneously integrated distributed feedback quantum cascade lasers on silicon," Photonics **3**, 35 (2016).
139. B. Kumari, A. Barh, R. K. Varshney, and B. P. Pal, "Silicon-on-nitride slot waveguide: a promising platform as mid-IR trace gas sensor," Sens. Actuators B **236**, 759–764 (2016).
140. Y. Chen, H. Lin, J. Hu, and M. Li, "Heterogeneously integrated silicon photonics for the mid-infrared and spectroscopic sensing," ACS Nano **8**, 6955–6961 (2014).
141. J. Chiles and S. Fathpour, "Mid-infrared integrated waveguide modulators based on silicon-on-lithium-niobate photonics," Optica **1**, 350–355 (2014).
142. M. Nedeljkovic, R. Soref, and G. Z. Mashanovich, "Free-carrier electrorefraction and electroabsorption modulation predictions for silicon over the 1-14-μm infrared wavelength range," IEEE Photon. J. **3**, 1171–1180 (2011).